



1 **Modeling the smoky troposphere of the**  
2 **southeast Atlantic: a comparison to**  
3 **ORACLES airborne observations from**  
4 **September of 2016**

5 Yohei Shinozuka<sup>1,2</sup>, Pablo E. Saide<sup>3</sup>, Gonzalo A. Ferrada<sup>4</sup>, Sharon P. Burton<sup>5</sup>, Richard Ferrare<sup>5</sup>,  
6 Sarah J. Doherty<sup>6,7</sup>, Hamish Gordon<sup>8</sup>, Karla Longo<sup>1</sup>, Marc Mallet<sup>9</sup>, Yan Feng<sup>10</sup>, Qiaoqiao Wang<sup>11</sup>,  
7 Yafang Cheng<sup>12</sup>, Amie Dobracki<sup>13</sup>, Steffen Freitag<sup>14</sup>, Steven G. Howell<sup>14</sup>, Samuel LeBlanc<sup>2,15</sup>,  
8 Connor Flynn<sup>16</sup>, Michal Segal-Rosenhaimer<sup>2,15</sup>, Kristina Pistone<sup>2,15</sup>, James R. Podolske<sup>2</sup>, Eric J.  
9 Stith<sup>15</sup>, Joseph Ryan Bennett<sup>15</sup>, Gregory R. Carmichael<sup>4</sup>, Arlindo da Silva<sup>17</sup>, Ravi Govindaraju<sup>18</sup>,  
10 Ruby Leung<sup>16</sup>, Yang Zhang<sup>19</sup>, Leonhard Pfister<sup>2</sup>, Ju-Mee Ryoo<sup>2,15</sup>, Jens Redemann<sup>20</sup>, Robert  
11 Wood<sup>7</sup> and Paquita Zuidema<sup>13</sup>

12 <sup>1</sup> Universities Space Research Association, Columbia, Maryland, USA

13 <sup>2</sup> NASA Ames Research Center, Moffett Field, California, USA

14 <sup>3</sup> Department of Atmospheric and Oceanic Sciences, and Institute of the Environment and  
15 Sustainability, University of California, Los Angeles, California, USA

16 <sup>4</sup> Center for Global and Regional Environmental Research, The University of Iowa, Iowa City,  
17 Iowa, USA

18 <sup>5</sup> NASA Langley Research Center, Hampton, Virginia, USA

19 <sup>6</sup> Joint Institute for the Study of the Atmosphere and Ocean, Seattle, Washington, USA

20 <sup>7</sup> Department of Atmospheric Science, University of Washington, Seattle, Washington, USA

21 <sup>8</sup> School of Earth & Environment, University of Leeds, LS2 9JT, United Kingdom



- 1 <sup>9</sup> CNRM, Météo-France and CNRS, UMR 3589, Toulouse, France  
2 <sup>10</sup> Environmental Science Division, Argonne National Laboratory, Argonne, Illinois, USA  
3 <sup>11</sup> Center for Air Pollution and Climate Change Research (APCC), Institute for Environmental and  
4 Climate Research, Jinan University, 510632 Guangzhou, China  
5 <sup>12</sup> Minerva Research Group, Max Planck Institute for Chemistry, 55128 Mainz, Germany  
6 <sup>13</sup> Rosenstiel School of Marine and Atmospheric Science, University of Miami, Miami, Florida,  
7 USA  
8 <sup>14</sup> University of Hawaii at Manoa, Honolulu, Hawaii, USA  
9 <sup>15</sup> Bay Area Environmental Research Institute, Moffett Field, California, USA  
10 <sup>16</sup> Pacific Northwest National Laboratory, Richland, Washington, USA  
11 <sup>17</sup> NASA Goddard Space Flight Center, Greenbelt, Maryland, USA  
12 <sup>18</sup> Science Systems and Applications, Inc, Greenbelt, Maryland, USA  
13 <sup>19</sup> Department of Marine, Earth and Atmospheric Sciences, North Carolina State University,  
14 Raleigh, North Carolina, USA  
15 <sup>20</sup> School of Meteorology, The University of Oklahoma, Norman, Oklahoma, USA  
16 *Correspondence to:* Y. Shinozuka (Yohei.Shinozuka@nasa.gov) and P. Zuidema  
17 (pzuidema@miami.edu)

## 18 **Abstract**

19 The southeast Atlantic is home to well-defined smoke outflow from Africa coinciding  
20 vertically with extensive marine boundary-layer cloud decks, both reaching their climatological  
21 maxima in spatial extent around September. A framework is put forth for evaluating the  
22 performance of a range of global and regional aerosol models against observations made during  
23 the NASA ORACLES (ObseRvations of Aerosols above CLouds and their intEractionS) airborne  
24 mission in September 2016. The sparse airborne observations are first aggregated into 2° grid boxes  
25 and into three vertical layers: the cloud-topped marine boundary layer (MBL), the layer from cloud



1 top to 3 km, and the 3-6 km layer. Aerosol extensive properties simulated for the entire study  
2 region for all September suggest that the 2016 ORACLES observations are reasonably  
3 representative of the regional monthly average, with systematic deviations of 30% or less. All six  
4 models typically place the bottom of the smoke layer at lower altitudes than do the airborne lidar  
5 observations by 300-1400 m, whereas model aerosol top heights are within 0-500 m of the  
6 observations. All but one of the models that report carbonaceous aerosol masses underestimate the  
7 ratio of particulate extinction to the masses, a proxy for mass extinction efficiency, in 3-6 km.  
8 Notable findings on individual models include that WRF-CAM5 predicts the mass of black carbon  
9 and organic aerosols with minor (~10% or less) biases. GEOS-5 overestimates the carbonaceous  
10 particle masses in the MBL by a factor of 3-6. Extinction coefficients in the free troposphere (FT)  
11 and above-cloud aerosol optical depth (ACAOD) are 10-30% lower in WRF-CAM5, 30-50%  
12 lower in GEOS-5, 10-40% higher in GEOS-Chem, 10-20% higher in EAM-E3SM except for the  
13 practically unbiased 3-6 km extinction, and 20-70% lower in the Unified Model, than the airborne  
14 in situ, lidar and sunphotometer measurements. ALADIN-Climate also underestimates the  
15 ACAOD, by 30%. GEOS-5 and GEOS-Chem predict carbon monoxide in the MBL with small  
16 (10% or less) negative biases, despite their overestimates of carbonaceous aerosol masses. Overall,  
17 this study highlights a new approach to utilizing airborne aerosol measurements for model  
18 diagnosis.

## 19 **1. Introduction**

20 The combined radiative impact of shortwave-absorbing aerosol and its interactions with  
21 clouds, microphysical and radiative, are subject to large uncertainties over the southeast Atlantic  
22 (Myhre et al., 2013; Stier et al., 2013). Efforts to distinguish aerosol effects from meteorology  
23 using satellite and reanalysis data suggest that large radiative impacts can be attributed to the  
24 shortwave-absorbing aerosol (Adebiyi and Zuidema, 2018; Chand et al., 2009), but ultimately  
25 models are necessary for attributing radiative impacts to the underlying processes. Recent  
26 modeling studies have emphasized both the radiative impact of aerosol-cloud microphysical



1 interactions (Lu et al., 2018) and the effects of free-tropospheric stabilization by smoke (Gordon  
2 et al., 2018; Sakaeda et al., 2011). The model process uncertainty, to some extent, reflects the  
3 paucity of in situ measurements of aerosol properties in this complex region, in which aerosols  
4 and clouds typically occur in the same vertical column but are not necessarily co-located. The  
5 southeast Atlantic atmosphere has been known to include elevated levels of biomass-burning  
6 aerosol (BBA) since at least Fishman et al. (1991), with subsequent satellite studies documenting  
7 the spatial extent and optical depth of the BBA more extensively. These confirm that the southeast  
8 Atlantic contains a global maximum of BBA present over a bright surface (the underlying  
9 stratocumulus deck) (Waquet et al., 2013), resulting in a strong regional climate warming (de Graaf  
10 et al., 2014; Peers et al., 2015) that is currently not represented in large-scale models (Stier et al.,  
11 2013; Zuidema et al., 2016).

12 An analysis of surface-based sunphotometer data from Ascension Island (Koch et al., 2009)  
13 and a more extensive evaluation using space-based lidar data (Das et al., 2017), conclude that  
14 global aerosol models underestimate the amount of BBA brought by long-range transport over the  
15 Atlantic. More recent limited in situ aircraft observations on black carbon (BC) mass  
16 concentrations further confirm the model underestimate of BC over the remote southeast Atlantic  
17 (Katich et al., 2018). Katich et al. (2018) compare these observations to a suite of models  
18 assembled by the Aerosol Comparisons between Observations and Models (AEROCOM) project,  
19 an international initiative encouraging the rigorous comparison of models to observations by  
20 imposing standardizations, such as a single fire emissions inventory, that allow for more fruitful  
21 attribution of model differences.

22 The Das et al. (2017) and Katich et al. (2018) comparisons were against global aerosol  
23 models at their developmental stage in 2012 (Myhre et al., 2013). As aerosol models become more  
24 sophisticated, more parameterizations are being developed that relate aerosol optical properties to  
25 their composition and evolution with time. The aerosol optical properties, primarily the single  
26 scattering albedo (SSA) and the vertical structure of extinction, are critical determinants of the  
27 direct and semi-direct aerosol radiative effects. To date, with the exception of Katich et al. (2018),



1 no assessments have been made of the model optical and compositional properties over the smoky  
2 southeast Atlantic. This primarily reflects the paucity of in situ measurements over the southeast  
3 Atlantic. The South African Regional Science Initiative (SAFARI) in 2000-2001 provided  
4 important data sets but these were confined to the vicinity of the south African coast (Swap et al.,  
5 2003). These measurements also preceded organized international efforts to evaluate global  
6 aerosol models systematically.

7 Motivated in part by the desire to improve model representation of BBA over the southeast  
8 Atlantic, a series of field campaigns initiated in the United States, United Kingdom, France and  
9 South Africa have gathered aircraft- and surface-based in situ and remotely-sensed data sets in this  
10 climatically important region, beginning in 2016 (Zuidema et al., 2016; Redemann, et al., in  
11 preparation). The first deployment of the NASA ObseRvations of Aerosols above CLouds and  
12 their intEractionS (ORACLES) campaign took place in September of 2016. The month of  
13 September was chosen a priori because this month was thought to reflect the climatological  
14 maximum in the spatial extent of overlap of absorbing aerosols above the semi-permanent  
15 subtropical southeastern Atlantic stratocumulus deck within the annual cycle, based on satellite  
16 passive remote sensing (Adebisi et al., 2015). Of the two deployed planes, the NASA P3 was  
17 instrumented primarily with in situ instruments and flew in the lower- to mid-troposphere. The  
18 NASA ER2 flew at about 20 km altitude with downward-viewing remote sensors. Examples of  
19 their new insights include a multi-instrument assessment of SSA (Pistone et al., 2019) and the  
20 above-cloud aerosol optical depths (ACAOD) (LeBlanc et al., 2019).

21 An important decision made prior to the deployments was to devote approximately half of  
22 all the research flights to routine flights along a pre-established path. The value of unbiased in situ  
23 sampling is highlighted in Reddington et al. (2017) as part of the Global Aerosol Synthesis and  
24 Science Project. The approach of devoting flight hours specifically to routine flight plans, to  
25 facilitate model assessment was arguably first applied during the VOCALS (VAMOS Ocean-  
26 Cloud-Atmosphere-Land Study) experiment in the southeast Pacific (Wood et al., 2011; Wyant et  
27 al., 2010, 2015). The aircraft campaigns over the southeast Atlantic differ in that a larger altitude



1 range (up to 6 km) was sampled than during VOCALS, which focused largely on the cloudy  
2 boundary layer (Wood et al., 2011). Approximately half of the fifteen ORACLES 2016 flights  
3 sampled the truly remote southeast Atlantic directly above the heart of the major stratocumulus  
4 deck (Fig. 1; Klein and Hartmann (1993)). Other flights acquired more detailed characterization  
5 of the atmospheric vertical structure at the expense of a longer range, and tended to occur closer  
6 to the African coast. Data sets from these flights also contribute to this study.

7 This paper compares modeled aerosol products with ORACLES 2016 observations. Our  
8 study extends more deeply into evaluating the composition, size, and optical properties of the  
9 modeled smoke particles above the southeast Atlantic than has been possible to date (described  
10 further in Section 2.1). The six models participating in this exercise all strive to represent the  
11 smoky southeast Atlantic atmosphere (Mallet et al., 2019) and are either versions of the aerosol  
12 transport models used for in-field aerosol forecasts or global and regional models applied for  
13 assessing the climate impact of the smoke (Section 2.2). Spatiotemporal ranges surrounding the  
14 ORACLES flights are chosen to address data sampling challenges (Section 3). The extent to which  
15 the sampled data represent the climatological monthly-mean is assessed in Section 4. The model-  
16 observation comparisons along the flights begin with the smoke plume altitude (Section 5).  
17 Aerosol properties are then compared within fixed altitude ranges (Section 6). The findings  
18 common among the models and divergent ones are discussed (Section 7). A summary is provided  
19 in Section 8.

## 20 2. Observations and Models

### 21 2.1. Observations

22 The instruments and the observed/derived values are described in detail in the Appendix, with  
23 general descriptions provided here and summarized in Table 1. BC, a key smoke component  
24 strongly absorbing of shortwave absorption, is measured by the Single Particle Soot Photometer  
25 (SP2; see Section 9.1.1) and organic and sulfate aerosol masses by a time-of-flight aerosol mass



1 spectrometer (AMS; Section 9.1.2). Aerosol size affects both the optical and the cloud-nucleating  
2 properties of BBA. Particles with dry diameters between 60-1000 nm are measured with an ultra-  
3 high sensitivity aerosol spectrometer (UHSAS; Section 9.1.3). This allows us to determine the  
4 volumetric arithmetic mean diameter of the accumulation mode, the cube root of the volume-to-  
5 number ratio after the volume is divided by  $\pi/6$ .

6 In situ aerosol scattering is measured by a nephelometer, and aerosol absorption by a  
7 particle soot absorption photometer (PSAP), both at an instrument relative humidity (RH) that is  
8 typically below 40% (Section 9.1.4). From these measurements, extinction coefficient and SSA at  
9 530 nm as well as scattering and absorption Ångström exponents (SAE, AAE) across 450-700 nm  
10 are derived. A detailed comparison of the SSA values to those from other instruments is shown in  
11 Pistone et al., (2019).

12 Statistics of the aerosol intensive properties (SSA, AE, volumetric mean diameter and an  
13 extinction-to-mass ratio) are only calculated from individual measurements with the midvisible  
14 dry extinctions greater than  $10 \text{ Mm}^{-1}$ , thereby reducing the noise apparent at lower aerosol  
15 concentrations.

16 The NASA Langley Research Center High Spectral Resolution Lidar (HSRL-2; Section  
17 9.1.5), deployed from the ER2 during 2016, provides measurements of the aerosol extinction  
18 vertical profiles at 355 and 532 nm. The HSRL-2 employs the HSRL technique (Shiple et al.,  
19 1983) to measure calibrated, unattenuated backscatter and aerosol extinction profiles and also has  
20 a higher signal-to-noise ratio than the space-based lidars, so it can extensively sample the complete  
21 aerosol vertical structure of the aerosol. These mitigate the well-documented low signal-to-noise  
22 issue with the space-based CALIOP lidar (Kacenelenbogen et al., 2011; Liu et al., 2015; Lu et al.,  
23 2018; Pauly et al., 2019; Rajapakshe et al., 2017). One measure of the ACAOD is derived from  
24 the HSRL-2 532-nm measurements. Another is available from 4STAR (Section 9.1.6), a  
25 sunphotometer / sky-radiometer (LeBlanc et al., 2019) from the low-flying P3 when above cloud  
26 top.



1 We use particulate 532-nm backscattering coefficient and cloud top height, which are  
2 among the standard HSRL-2 products (Burton et al., 2012), to define the bottom and top heights  
3 of the smoke plumes. We set a threshold particulate backscattering coefficient at  $0.25 \text{ Mm}^{-1}\text{sr}^{-1}$ .  
4 For the layer bottom, we do not search within 300 m of the layer top or beneath the cloud top  
5 height. Our statistics do not include the cases where the smoke base is identified to be higher than  
6 4 km, to avoid artefact noise due to imperfectly cleared cirrus. The extinction threshold is  
7 approximately equivalent to an extinction of  $15 \text{ Mm}^{-1}$  for an estimated extinction-to-backscattering  
8 ratio of 60 sr and to a BC mass concentration of  $200 \text{ ng m}^{-3}$  at standard temperature and pressure  
9 (STP, 273K and 1013 hPa) For model output we use this BC value as the smoke plume threshold,  
10 as this property is inherent to biomass burning and because the models do not produce  
11 backscattering (the lidar backscattering method does not distinguish between smoke and other  
12 aerosols such as marine aerosol). These are conservative choices emphasizing the clear presence  
13 of smoke (57% of the 60s-average SP2 measurements in the free troposphere (FT) exceed  $200 \text{ ng}$   
14  $\text{m}^{-3}$  STP). Though not explored in the current analysis, the subjective choice will affect the gap  
15 distance between the smoke plume bottom and the cloud top.

16 Carbon monoxide (CO), a tracer for air masses originating from combustion, is measured  
17 by a Los Gatos Research CO/CO<sub>2</sub>/H<sub>2</sub>O Analyzer (Section 9.1.7). Overall these variables are  
18 selected because they are robustly-observed, are pertinent to the absorption of shortwave  
19 radiation and are available in most models. Cloud condensation nuclei number concentrations  
20 organic carbon (a derived quantity from the AMS measurements) and cloud properties are not  
21 compared in this study.

## 22 2.2. Models

23 The six assessed models are summarized in Table 2 and detailed in the Appendix. The  
24 models are assessed using their native parameterizations and emission inventories, with no  
25 standardization applied across the models, in contrast to the planned experiments of the  
26 AEROCOM initiative. The primary ORACLES aerosol forecast tools are a version of the regional



1 WRF-CAM5 model (Section 9.2.1) possessing simpler aerosol microphysics (WRF-AAM, WRF  
2 with aerosol-aware microphysics (Diamond et al., 2018; Saide et al., 2016)) and the NASA GEOS-  
3 5 global aerosol model (Section 9.2.2). Additional analysis is performed with these two models to  
4 assess whether the in situ data from the flight days are representative of the monthly-mean  
5 distributions more typical of Intergovernmental Panel on Climate Change studies. The WRF-  
6 CAM5 model is also the only model containing all of the aerosol variables with complementary  
7 aircraft measurements.

8 The UK Unified Model (UM; Section 9.2.5) in its numerical weather prediction  
9 configuration produced forecasts for the CLARIFY campaign in 2017, with simpler smoke aerosol  
10 emissions and microphysics than that assessed within the current study. The three other state-of-  
11 the-art models are GEOS-Chem (Section 9.2.3), EAM-E3SM (Section 9.2.4) and the ALADIN-  
12 Climate (Section 9.2.6; also assessed within Mallet et al. (2019)).

13 A threshold of  $200 \text{ ng m}^{-3}$  of BC mass concentration at STP is used to locate the model  
14 smoke plumes. The only exception is ALADIN-Climate, for which an extinction threshold of  $17$   
15  $\text{Mm}^{-1}$  is used. As with the observations, the model intensive properties are only aggregated using  
16 data with 550 nm extinctions (under dry conditions if reported otherwise under the ambient  
17 humidity) greater than  $10 \text{ Mm}^{-1}$ . The volume mean diameter is computed from the accumulation  
18 mode only, as smaller aerosol sizes contribute little to the overall aerosol number and mass.

### 19 **3. Framework for the Model-Observation Comparison**

#### 20 **3.1. Vertical Ranges**

21 The analysis is performed in three altitude ranges: the cloud-topped marine boundary layer  
22 (MBL), the region above the cloud top up to 3 km, and from 3 to 6 km. During September 2016,  
23 within the sampled domains, the cloudy boundary layer is materially separated from the much  
24 drier FT by a strong inversion, evident in aircraft RH profiles (Fig. 2). For the in situ observations  
25 available from the P3, we define the MBL as altitudes below  $(\text{RH}(\%) - 60) * 40 \text{ m}$ . This definition



1 is useful in that it does not require a vertical gradient, which is only available for limited flight  
2 segments.

3 For models, the basic definition of the MBL top height is the level where the vertical  
4 derivative of the specific humidity with respect to altitude is a minimum. The basic concept is to  
5 define the depth of the layer where the surface has significant immediate influence on the moisture.  
6 This depth is often larger than the traditional “well-mixed” region where the potential temperature  
7 is nearly constant. To take into account differences in boundary layer dynamics between land and  
8 ocean, and between the northern (latitude north of 5°S) and southern regions, we implement some  
9 modifications to this basic scheme. First, we calculate  $dq/dz$ , where  $q$  is specific humidity and  $z$  is  
10 altitude, at all grid points up to the level  $D$ . Here  $D$  is 3 km over oceanic regions and 6 km over  
11 land (small islands in the SE Atlantic, e.g., St Helena and Ascension, are considered oceanic).  
12 Next, we find the altitude  $z_0$  where  $dq/dz$  is a minimum. The different altitudes  $D$  for land and  
13 ocean are chosen because: (1) boundary layers (even the well-mixed convective boundary layer)  
14 on the African continent are often quite deep, up to 5 km; and (2) occasionally the  $dq/dz$  minimum  
15 over the oceans is at the top of the smoke layer (so we restrict the MBL depth to a maximum of 3  
16 km). For our model sampling of the MBL, we use data from the surface up to half the height of  
17 the MBL to avoid the possibility of cloud artifacts.

18 The two definitions of the cloud-topped MBL differ only slightly within the WRF-CAM5  
19 model, in which the RH-based definition places the top of the MBL 120 m higher than the gradient-  
20 based one, in the mean. An interest in facilitating future model-observation intercomparisons from  
21 2017 and 2018 aircraft data taken in more equatorward regions of the southeastern Atlantic, where  
22 cloud cover is lower and clouds are more multi-layered, justifies the use of the two MBL height  
23 definitions.

24 For both observations and models, the altitude of 3 km is chosen to distinguish the lower  
25 and mid FT. The lower FT, up to 3 km, contains aerosols that are more likely to mix into the MBL  
26 over the southeastern Atlantic at some future time (Diamond et al., 2018). In contrast, the only  
27 interaction of aerosols in the upper 3-6 km layer with the underlying cloud deck is through



1 radiation. Note that for the lower FT, we require that the ambient RH be below 60% and the altitude  
2 at least 500 m, to exclude the observations in the MBL. HSRL-2 observations generally show a  
3 better defined plume with larger aerosol loads in the mid FT than in the lower FT, the latter often  
4 separated from the cloud top (Burton et al., 2018).

### 5 **3.2. Horizontal and Temporal Ranges**

6 An additional challenge for any model evaluation using observations, especially in situ, is  
7 the scale mismatch. The in situ measurements are collected at spatial scales of approximately one  
8 sample per ~100 m, one location at a time. In contrast, the model values represent averages over a  
9 horizontal grid spacing of tens of kilometers, available at regular intervals. The sampling bias is  
10 dealt with by aggregating the data from both the observations and models into 2°-by-2° latitude-  
11 longitude boxes and slightly larger ones (Fig. 3). Box-whisker plots summarize the full range of  
12 the distribution through reporting the 10th, 25th, 50th (the median), 75th and 90th percentiles as  
13 well as the means and standard deviations. This approach is similar to that applied within  
14 AEROCOM studies (Katich et al., 2018) but the data aggregation occurs within smaller domains  
15 and aims to capture regional spatial gradients, similar to Wyant et al. (2010, 2015).

16 Observations are first averaged over one minute from their native values, to limit the small-  
17 scale variability and instrumental noise. A one-minute mean is equivalent to an approximate  
18 horizontal scale of 7-10 km at the typical P3 aircraft speed and 12 km at the typical ER2 speed.

19 One of the three main corridors encompasses the routine flight track, with individual grid  
20 boxes centered at (14° E, 24° S), (12° E, 22° S), (10° E, 20° S), (8° E, 18° S), (6° E, 16° S), (4° E, 14°  
21 S), (2° E, 12° S) and (0° E, 10° S), each having corners at 2° north, east, south and west, respectively,  
22 of the center. Another, coastal north-south corridor has the southernmost grid box centered on 22°  
23 S, spanning between 9° E and 11.75° E. Seven grid boxes are located every 2° north of this, with  
24 the northernmost grid box centered on 8° S. A third, west-east corridor covers the larger domain  
25 of the ER2 measurements, with individual grid boxes spanning latitudinally between 10° S and 6°  
26 S and separated longitudinally at 2° intervals beginning at 3° W to the west and 13° E in the east.



1 The box for St. Helena Island spans between  $6.72^{\circ}$  W and  $4.72^{\circ}$  W, between  $16.93^{\circ}$  S and  $14.93^{\circ}$   
2 S.

3 All P3 and ER2 flights occurred during daytime, with data primarily gathered between 9  
4 am to 4 pm in Central Africa Time (7 am to 2 pm UTC). The P3 sampled for 96 hours in the  
5 diagonal and meridional corridors. The ER2 sampled for 30 hours in these domains and 8 hours in  
6 the zonal corridor. The models are sampled at the three-hourly times closest to those of the  
7 measurements, except for the climatology study presented in Section 4. Diurnal variations in  
8 aerosol properties are small and not considered.

#### 9 **4. Representativeness of the Airborne Sampling**

10 An a priori analysis based on MODIS clear-sky aerosol optical depths indicates that the  
11 ORACLES sampling is sufficient to capture the monthly mean. A posteriori analysis based on  
12 WRF-CAM5 and GEOS-5 model output of aerosol extinctions, presented below, confirms this.  
13 The daytime model outputs for the whole month of September occurring within the defined grid  
14 boxes are compared to the smaller data set of model output sampled closest in space and time to  
15 the observations.

16 The WRF-CAM5 model aerosol extinctions between 3-6 km altitudes corresponding to  
17 the days when the HSRL-2 extinctions are available (Fig. 4a, blue boxes and whiskers) generally  
18 agree well with the values based on the entire month (black boxes and whiskers). The same can be  
19 said for the comparison based on the P3 flight days (Fig. 4b). This is true for both the diagonal and  
20 meridional corridors (left and right halves, respectively, of each panel). This conclusion is based  
21 on an evaluation of the mean bias (MB) and the root-mean-square deviations (RMSD) for the two  
22 model populations. The MB between the monthly-mean and flight-day-only means is between -  
23 10 % and +10 % of the monthly means. The RMSD based on the model output from the flight  
24 days only are 20-30 % of the monthly-mean values for each aircraft. The MB and RMSD values  
25 are provided in Table 3 for the two aircraft and three layers. The MBL (Fig. 4d) MB and RMSD  
26 values are similar to those for 3-6 km. In the layer extending above MBL up to 3 km (Fig. 4c), the



1 means of the extinction modeled along the P3 flight tracks exceed the monthly means on the  
2 diagonal corridor and at the southern half of the meridional corridor, by approximately 20 % across  
3 the boxes. Comparisons based on BC, organic aerosol (OA), CO and ACAOD are mostly similar  
4 to those based on the light extinction. The only exception occurs within the MBL, wherein the  
5 mean BC and OA mass concentrations on flight days exceed the monthly-mean values by  
6 approximately 30-40 % (Table 3). In-flight sampling decisions favoring more smoky conditions  
7 may be responsible for this bias.

8 This analysis is used to assess if the observations gathered on flight days are representative  
9 of the monthly-mean spatial trends across the southeast Atlantic, at the different vertical levels.  
10 The FT of the southern end of the sampled domain is less smoky in the mean than the northern  
11 end (LeBlanc et al., 2019), the latter being closer to the main smoke outflow of the region at  $\sim 10^\circ$   
12 S. The flight days capture the spatial trend well in the mid troposphere and MBL, and somewhat  
13 less so in the lower FT especially near the coast.

14 Results from GEOS-5 for the in situ properties for 3-6 km and MBL and the ACAOD are  
15 similar to those from WRF-CAM5 in terms of the climatology representativeness. The magnitude  
16 of the MB in 3-6 km is slightly smaller, at 5 % or less (Table 3). For the lower FT (above MBL-3  
17 km), GEOS-5 shows that ORACLES flights sampled lighter aerosol loading than the month-long  
18 average, by about 10 %, while WRF-CAM5 shows heavier smoke loads as mentioned above. The  
19 discrepancy between the two models is related to the way each model identifies the smoke bottom  
20 height. While GEOS-5 sees little systematic difference (+100 m) for the ORACLES flights  
21 compared to the climatology, in WRF-CAM5 the smoke bottom height was about 400 m higher,  
22 on average (Table 3).

23 To summarize, comparisons between the aerosol loadings within the WRF-CAM5 and  
24 GEOS-5 simulations from flight-days-only to those from the full month suggest that the MBL  
25 aerosol loading sampled during the 2016 ORACLES flights likely exceeded monthly-mean values.  
26 WRF-CAM5 and GEOS-5 disagree as to whether the lower FT had heavier or lighter aerosol  
27 loadings on flight days than the monthly-mean. We note, however, that the mean biases are



1 generally between -10 % and +30 % in the lower FT and MBL, and less within the 3-6 km layer.  
2 To this extent the ORACLES observations, at least in the diagonal and meridional corridors,  
3 represent the regional climatology for September 2016.

## 4 **5. Evaluation of Model Aerosol Plume Heights**

5 An initial evaluation of the free-tropospheric aerosol layer top and bottom altitudes  
6 prepares for the comparisons carried out for the comparison layers. The HSRL-2 observations  
7 indicate that smoke layer top is highest, 5-6 km, between 9-17° S (Fig. 5a). The mean aerosol bases  
8 are typically located at 1.5-2.5 km rising slightly from north to south. The observed plume top and  
9 bottom heights show little zonal gradient along 8° S (Fig. 5b):  $1740 \pm 290$  m for the bottom and  
10  $5250 \pm 180$  m for the top, the value after the  $\pm$  symbol expressing the standard deviation among  
11 the mean altitudes of the 2° grid boxes between 3° W and 13° E.

12 All of the models tend to place the smoke plume at a lower altitude than the HSRL-2,  
13 especially in the northern half of the area. GEOS-5 and GEOS-Chem underestimate the mean top  
14 heights most severely, with an MB of -500 m for both. The negative bias does not exceed 200 m  
15 for UM, EAM-E3SM, WRF-CAM5 and ALADIN-Climate (Fig. 5, Table 3). These biases are less  
16 than the model vertical resolution at these altitudes (e.g., WRF-CAM5 has ~500 m layer thickness  
17 at 5 km altitude) so that at least the <200m underestimates are within the expected model  
18 uncertainty.

19 The underestimates in the aerosol layer bottom heights are more diverse (300-1400 m)  
20 among the models. The MB is more negative than for the top height for each of the models, i.e.,  
21 all models generally overestimate the smoke plume vertical thickness. As with the top heights, the  
22 GEOS-Chem and GEOS-5 models underestimate the bottom altitudes most severely.

23 Despite generally placing the FT aerosol layers too low, most models are able to capture  
24 an equatorward increase in the aerosol layer tops, and an opposite gradient in the layer bases. Most  
25 models skilfully locate the maximum aerosol layer tops at 13-15°S close to the coast (the  
26 meridional corridor). One exception is ALADIN-Climate, which overall underestimates the top



1 height by ~500 m but overestimates further to the south. As a result, while the bias is small, the  
2 variability between the grid boxes is somewhat greater (RMSD 800 m) than for WRF-CAM5 (400  
3 m), UM (400 m) and EAM-E3SM (500 m) and is closer to that for GEOS-5 (600 m) and GEOS-  
4 Chem (800 m).

5 The variability is generally predicted too low within the southernmost boxes. The observed  
6 smoke heights near 20° S are more variable than further north, possibly related to more complex  
7 (re)circulation patterns away from the primary jet outflow core. The models have more difficulty  
8 representing this variability and do not necessarily capture the spatial trends in the smoke heights.

## 9 **6. Evaluation of Models at Bulk Vertical Levels**

10 The six models are compared against the observations within the three pre-defined bulk  
11 vertical layers using box-whisker plots to capture the mean and the variability. Comparisons for  
12 the diagonal corridor are shown to the left of the meridional one in Figs. 6-14. The mean bias and  
13 standard deviations of each of the model products from the observations are summarized in Table  
14 4. The model products provided in this section are sampled near the location and time of the  
15 airborne measurements, not monthly values.

### 16 **6.1. Aerosol Chemical and Physical Properties**

17 Fig. 6 compares the observed versus modeled BC mass concentrations at the ambient  
18 temperature and pressure for the five reporting models. In the mid FT (3-6 km altitude; Fig. 6a),  
19 the WRF-CAM5 model (blue color) is in the best agreement with the SP2 observations (black),  
20 with an RMSD between the 16 grid box means of 170 ng m<sup>-3</sup>. The agreement of the GEOS-5  
21 (orange) model with the measurements is slightly poorer, with an RMSD of 210 ng m<sup>-3</sup>. These  
22 values are around 30 % of the mean observed values, as noted in parentheses in Table 4. Little  
23 systematic bias is discernible in the figure. The MB of the box means is as small as +10 % (Table  
24 4).



1 In contrast, GEOS-Chem has practically zero MB but an RMSD that is 50 % of the mean  
2 (Fig. 6, green) due to underestimates in the northern half of the diagonal corridor (NW-SE boxes)  
3 away from the land (the left half of the panel) and overestimates nearer the coast (the right half).  
4 This shift is consistent with the increasing underestimate in the smoke top height as the plume  
5 advects towards the west in this model (Fig. 4). UM and EAM-E3SM underestimate BC mass  
6 concentrations in the 3-6 km layer by 40-50 % in all regions, with this systematic bias driving the  
7 RMSD.

8 Above the MBL up to 3 km (Fig. 6b), the models typically underestimate the BC loading  
9 further offshore and to the north, and agree better with the observations towards the south, where  
10 less smoke is present. The strong observed gradient from south to north is not represented in most  
11 models. The model-observation RMSD is greater in the lower FT than in the mid FT for WRF-  
12 CAM5 (60 %), GEOS-5 (60 %) and EAM-E3SM (80 %). GEOS-Chem performs in this layer  
13 similar to its performance in the 3-6 km layer, with an RMSD of 50 % and no apparent bias. UM  
14 underestimates less severely in this layer (-20 % MB) than in 3-6 km.

15 Much less BC is observed in the MBL (Fig. 6c) than in the FT. GEOS-5 overestimates  
16 MBL BC, more significantly (+160 % MB) than in the FT (+10-20 %), as does GEOS-Chem.  
17 EAM-E3SM shows better agreement with observations in the MBL than above it. WRF-CAM5  
18 and UM do not noticeably skew the BC vertical distribution towards the MBL. WRF-CAM5  
19 overestimates in the northernmost boxes on the diagonal corridor, but by less than GEOS-5 does.

20 Measured organic aerosol (OA) mass concentrations at the ambient temperature and  
21 pressure, shown in Fig. 7, increase from south to north near the coast, with concentrations lower  
22 further offshore. The models capture this trend, but show somewhat greater deviations in OA than  
23 in BC. The RMSD in the 3-6 km layer, for example, is around 40 % for WRF-CAM5, 90 % for  
24 GEOS-5, 60 % for GEOS-Chem, 100 % for EAM-E3SM and 50 % for UM.

25 In the lower FT the GEOS-5 OA is more than twice that observed, and in the MBL more  
26 than six times. The biases are more positive in the MBL than in the FT in all models. For both BC  
27 and OA, the RMSD is also greater at lower altitudes.



1            Only two models (WRF-CAM5 and the UM) report an aerosol diameter. The diameter of  
2 the emitted aerosol is prescribed within these models, and allowed to evolve thereafter. The  
3 measured volumetric mean dry aerosol diameters from the UHSAS are close to 200 nm, with little  
4 geographical or altitude variation.

5            The UM volumetric mean diameter is greater than the observation by 60-70 nm in the FT.  
6 The modeled diameters are 20 % greater in the ambient RH. In the MBL the UM-observation  
7 differences in diameter are marginally smaller, especially on the diagonal corridor. WRF-CAM5  
8 volumetric mean aerosol diameters, which are calculated for the dry conditions, exceed measured  
9 values by 40-80 nm in the FT and by 100 nm in the MBL (Fig. 8). The cause is a prescribed  
10 volumetric geometric mean diameter of 375 nm for the emitted accumulation mode particles (the  
11 geometric standard deviation is 1.8). Future simulations will use diameters closer to that  
12 representative of biomass burning emissions.

## 13            **6.2. Aerosol Optical Properties**

14            Fig. 9 shows model-derived ACAOD compared to observed mid-visible wavelength values  
15 from the ER2-borne lidar and the P3-borne sunphotometer. The WRF-CAM5 ACAOD values are  
16 biased low, by 10-20 % (Fig. 9, Table 4), particularly in the northern region closer to the plume  
17 core. Underestimates by GEOS-5 and ALADIN-Climate are larger still (~30-40 %) and EAM-  
18 E3SM overestimates by 20 %. While these models show similar degrees of deviations for the two  
19 instruments, GEOS-Chem overestimates by 40 % for the HSRL-2 but only by 5 % for 4STAR.

20            Model differences from the observed mid-visible light extinction (Fig. 10) broadly follow  
21 those for ACAOD. The top panel shows lidar-derived extinction at ambient RH, while the other  
22 three panels show the sum of nephelometer scattering and PSAP absorption coefficients measured  
23 at low (~20 %) RH. For both comparisons the model values refer to ambient RH. In the FT, the  
24 ambient-RH/dry ratio of light scattering is estimated to be less than 1.2 for the 90 % of the time  
25 when the dry scattering exceeds  $1 \text{ Mm}^{-1}$ , according to concurrent, once-per-second measurements  
26 with two nephelometers with instrument RH set respectively to high (~80 %) and low (~20 %). In



1 contrast, in the MBL, where the relative humidity typically exceeds 85 % and the aerosols are  
2 more hygroscopic, the effect of aerosol hygroscopic swelling on the extinction is pronounced,  
3 exceeding 2.2 for half of our measurements. Thus, while the WRF-CAM5 extinctions are  
4 systematically lower (by 30 %) relative to the in situ values in both mid FT and MBL, the  
5 underestimate in extinction within the MBL is in practice more severe. Since the WRF-CAM5  
6 model predicts RH with little bias, the severe underestimate may be due to poor representation of  
7 the aerosol properties within the MBL. The comparison to the HSRL-2 ambient extinction only  
8 shows a 20 % underestimate. This could be due to the sampling bias in the in situ observation,  
9 although the differences in the locations and sampling time between the two aircraft preclude a  
10 definitive conclusion.

11 GEOS-5 underestimates the FT extinction to a greater degree than does WRF-CAM5, by  
12 30-50 %, but grossly overestimates extinction within the MBL. GEOS-Chem shows biases to the  
13 positive direction in the MBL (+130 %) and in the FT (by 10-30 %). EAM-E3SM indicates smaller  
14 overestimates (~10 % or smaller in magnitude) in the FT, with values in the northern half of the  
15 near-coast corridor particularly close to the observation. The overestimate in the MBL by EAM-  
16 E3SM is even more severe than that by GEOS-5. UM generally underestimates the extinction, by  
17 30 % compared to the lidar extinction on the ambient humidity basis and by 40-80 % compared to  
18 the in situ extinction on the dry basis.

19 The Ångström exponent of scattering is another, independent if indirect measure of particle  
20 size that is more readily available from the models included here than is the aerosol size itself. The  
21 Ångström exponent is computed as the slope of a linear fit of the scattering versus wavelength on  
22 logarithmic scales for cases where the 550 nm extinction exceeds  $10 \text{ Mm}^{-1}$ . Large Ångström  
23 exponents tend to correspond to smaller particle sizes. The scattering Ångström exponent is  
24 systematically underestimated by WRF-CAM5, by an absolute value of 0.6-0.8 (Fig. 11),  
25 consistent with the overestimated aerosol mean sizes (Fig. 8). UM, GEOS-5 and GEOS-Chem  
26 agree better with the observed values in the FT, with an RMSD of 0.1. The largest deviations are  
27 found in the northern end of the near-coast flights where the observations are relatively sparse.



1 Within the MBL, all of the models tend to underestimate the scattering Ångström exponent,  
2 indicating model particle sizes that are larger than observed.

3 The absorption Ångström exponent differs from the scattering Ångström exponent in that  
4 it is primarily a function of particle composition, and secondarily of particle size. In the FT the  
5 absorption Ångström exponent is systematically underestimated by 0.1 in the UM for dry aerosols,  
6 by 0.4-0.5 in WRF-CAM5, GEOS-5 and GEOS-Chem (Fig. 12). The modelled flatter spectra may  
7 reflect model overestimates in BC absorption or underestimates in absorbing organic material or  
8 dust. The models have very small ranges in the absorption Ångström exponent, both within each  
9 of the comparison boxes and across them.

10 SSA is key to establishing the radiative impact of the aerosol layer. The dry in situ  
11 observations indicate midvisible SSA values of 0.85 to 0.89 in the mid FT and 0.80 to 0.86 in the  
12 lower FT. SSA in the lower FT (Fig. 13b) is simulated by WRF-CAM5 and GEOS-5 well, with  
13 minor biases (+0.01 or smaller) and RMSD of 0.01-0.02. In the mid FT (Fig. 13a), WRF-CAM5  
14 systematically underestimates SSA by 0.03. GEOS-5 also underestimates it, but by noticeably  
15 smaller margins near the coast. GEOS-Chem overestimates SSA most severely, by 0.07-0.08 in  
16 both layers. EAM-E3SM also overestimates by 0.08 in the lower FT, by 0.02 in the mid FT.  
17 However, all of these models diagnose SSA in ambient conditions, while the observations are in  
18 dry conditions. The UM predicts both, and while the ambient simulated SSA also agrees  
19 reasonably well with the dry observations, the SSA for dried particles in the FT is underestimated  
20 by 0.07 in mid FT and 0.03 in lower FT. The models generally overestimate SSA in the MBL (Fig.  
21 13c), but this assessment is subject to particularly poor statistics due to the scarcity of cases with  
22 dry extinction exceeding  $10 \text{ Mm}^{-1}$  and the lack of adjustment for the humidity effect.

### 23 **6.3. Carbon Monoxide**

24 We also compare CO mixing ratio from the three models reporting it to measured quantities  
25 (Fig. 14). The measurements range from 60 ppbv to over 500 ppbv. The three models tend to  
26 underestimate, especially further offshore in 3-6 km and in the northern half of the near-coast



1 corridor. WRF-CAM5 systematically underestimates by ~20 % in the FT, as does GEOS-5 to a  
2 lesser degree (~10 %), with GEOS-Chem somewhere in between. In the MBL, where the observed  
3 mixing ratio is typically below 130 ppbv, the models also typically predict low, most notably near  
4 the southern end and near the coast. GEOS-Chem shows an altitude dependence in MB (-20 % in  
5 3-6 km, -5 % below), but the dependence is not as strong as that seen in the carbonaceous masses.  
6 The relative RMSD, at 20-30 % for these models, is smaller than for any of the aerosol extensive  
7 properties.

## 8 **7. Discussion**

9 The six models in this study have several common features, most notably the underestimate  
10 of the smoke bottom height. The models diverge widely on other properties, such as the magnitude  
11 of carbonaceous aerosol masses and light extinction. Here we discuss the results with respect to  
12 the model representations of the smoke emission, transport and mass extinction efficiency.

13 The low biases of smoke heights are a consequence of skewed aerosol mass vertical  
14 profiles. As the heights are determined with BC in all models but one, the model that most severely  
15 overestimates the masses (both BC and OA) in the MBL, GEOS-5, most severely underestimates  
16 the smoke height. The model that underestimates the height least severely, WRF-CAM5 (setting  
17 aside ALADIN-Climate which does not produce the masses), overestimates the MBL masses least  
18 severely. Another manifestation of the difficulty in representing the plume base is the generally  
19 greater random deviations, expressed as RMSD, in the carbonaceous masses at lower FT and MBL.

20 The low bias of the smoke layer heights has previously been attributed to an overestimate  
21 of the subsidence over the ocean (Das et al., 2017), an underestimate in the smoke injection heights  
22 at the source (Myhre et al., 2003) and the dry deposition velocity scale factor (Regayre et al.,  
23 2018). Of these, an exaggerated subsidence over the ocean would not only influence the transport  
24 of smoke but also the top height of clouds. Often the smoke base height is determined by the cloud  
25 top height in models, as smoke concentrations in the MBL are usually below the threshold used  
26 for defining the smoke boundaries. If models underestimate cloud top heights for stratocumulus



1 decks, as they often do in the southeast Pacific (Wyant et al., 2015), that could contribute to the  
2 smoke bottom underestimates and diversity. But it is not clear whether subsidence fully explains  
3 the underestimates by as large as 1400 m.

4 Neither do subsidence and injection heights explain another common feature in the present  
5 study: the three models that provide CO neither dramatically overestimate it in the MBL nor skew  
6 its vertical distribution towards lower layers relative to the observations. This is internally  
7 consistent for WRF-CAM5 where the altitude dependence is also small for OA and virtually non-  
8 existent for BC. For GEOS-5 and GEOS-Chem the altitude dependence is strikingly different  
9 between the carbonaceous aerosol masses and CO.

10 Fig. 15a-c illustrate this disconnection on a pre-aggregation basis (i.e., 60s means). BC and  
11 CO are compared on logarithmic scales in order to show the entire range of values including low  
12 CO cases common in the MBL. The logarithmic scales and the use of geometric mean and standard  
13 deviation later in the discussion also handle the ratios (of aerosol masses to CO) better, by keeping  
14 the average ratio and the ratio of averages identical to each other.

15 The observed relationship (Fig. 15a) is tight for CO above 130 ppb. Most of these data  
16 points occur in the FT (grey dots). Most MBL observations (blue) show CO between 60-130 ppbv.  
17 In this range the relationship with BC is less tight, probably because smoke, upon entering MBL  
18 clouds, loses aerosols to wet scavenging. BC is lower than  $500 \text{ ng m}^{-3}$  in the MBL in almost all  
19 cases, and is often as small as  $10 \text{ ng m}^{-3}$ . WRF-CAM5 shows a similar BC-CO relationship (Fig.  
20 15b). The only notable deviation from the observations is in the somewhat smaller diversity in  
21 carbonaceous aerosol masses, evident as a function of the CO (Fig. 15) and by location (box-  
22 whiskers in Fig. 6 and 7).

23 GEOS-5 (Fig. 15c, note the fewer data points due to the larger grid boxes), on the other  
24 hand, has high BC values in the MBL with values exceeding  $100 \text{ ng m}^{-3}$  in most cases with  
25 excursions up to  $1000 \text{ ng m}^{-3}$ . The relationship between OA and CO is qualitatively similar (Fig.  
26 15f). The somewhat higher scatter of the data points suggests that the degrees of secondary



1 condensation and chemical aging processes vary significantly, since OA is subject to these  
2 processes whereas BC is not.

3 If the degrees of mixing of smoke into the MBL were the only source of error, the aerosol  
4 masses and CO would be biased by similar proportions. The combinations of these two variables  
5 would be on or near the observed relationships. But they are not, as the figure shows. Additional  
6 factors must drive GEOS-5 (and GEOS-Chem) to produce anomalously high BC, but not CO. The  
7 only process that is known to significantly affect CO, removal through oxidation and cloud uptake,  
8 is negligible on the timescale of advection (a few days to two weeks) from the African biomass  
9 burning regions. Spatiotemporal sampling bias, positive and small (+20 % relative to the regional  
10 September average (Section 4)), does not explain the BC overestimates by a factor of 3.

11 With these possibilities excluded, we expect that processes influencing aerosols in an  
12 altitude-dependent manner but not CO must be the primary reason. Aerosol removal processes  
13 may be misrepresented, although Das et al. (2017) found that those in GEOS-5 contributed little  
14 to the differences they observed. Other possible explanations are secondary formation, coagulation  
15 and condensation.

16 EAM-E3SM and UM generally underestimate the BC masses in the FT. While model  
17 uncertainty in representing aerosol removal and transport cannot be excluded, the most likely cause  
18 is an overall underestimate of the smoke aerosol mass. In particular, in EAM-E3SM, monthly  
19 biomass burning emissions for an average year, mean of 1997-2000, are used, which dampen the  
20 model's ability to faithfully reproduce episodic burning events. Low emissions could also arise  
21 from the insensitivity of satellite retrievals to very small fires (Fornacca et al., 2017; Petrenko et  
22 al., 2017; Zhu et al., 2017).

23 For OA, factors other than emission seem to be at play. The altitude of OA is biased low  
24 in all models, more significantly than that of the less hygroscopic BC. Assuming negligible  
25 systematic biases in the observations, this may be due to insufficient wet removal in the model  
26 MBL. Consistently, the EAM-E3SM also puts significantly more sulfate (relative to the  
27 observations) towards the MBL, although WRF-CAM5 and UM do not. Another possible



1 explanation is in the representation of SOA. In the UM all monoterpene emissions are at the surface  
2 with no representation of plumes, and the lifetime of SOA may be too short for it to be elevated.  
3 EAM-E3SM includes a slower yield-based SOA formation from six gaseous precursors (Liu et al.,  
4 2012), but the SOA formation in the southeast Atlantic has not been evaluated.

5 The extinction coefficient in the FT and ACAOD within GEOS-5 and WRF-CAM5 are,  
6 counterintuitively, underestimated while the masses are generally overestimated. This is partly  
7 because some aerosol components beyond BC, OA and sulfate are not incorporated into the  
8 models. WRF-CAM5, for example, does not compute nitrate and ammonium, which contribute  
9 9% and 5%, respectively, to the total aerosol mass as observed with the AMS and SP2.

10 Nevertheless, the missing aerosol mass components are too small to fully account for the  
11 extinction underestimates. Sampling measurement bias is unlikely to fully explain the discrepancy,  
12 because the modeled extinction is also biased by -10% against the better-vertically-sampled  
13 HSRL-2 observations whose higher abundance reduces sampling bias (ER2 flights without HSRL-  
14 2 measurements are excluded from our study). We therefore conclude that the mass extinction  
15 efficiency (MEE) implicit in these models must be underestimated.

16 While the missing mass components prevent us from computing MEE in the models, the  
17 ratio of extinction to carbonaceous masses (OA+BC) can illustrate its spatial and inter-model  
18 variabilities in an approximate manner, provided that biomass-burning particles dominate the  
19 aerosol mass and extinction (which is the case in the biomass-burning plume in the FT). The quasi-  
20 MEE calculated from the box mean ambient extinction and masses in the FT is shown in Fig. 16.  
21 Each model takes a fairly constant value across the locations. In the lower FT, WRF-CAM5,  
22 GEOS-Chem, EAM-E3SM have values near  $8 \text{ m}^2\text{g}^{-1}$ . UM Ambient has  $6 \text{ m}^2\text{g}^{-1}$ .

23 In 3-6 km, the modeled quasi-MEE values show wider inter-model spreads. While WRF-  
24 CAM5 and GEOS-Chem have  $8\text{-}10 \text{ m}^2\text{g}^{-1}$ , EAM-E3SM and UM Ambient indicate values closer  
25 to  $6 \text{ m}^2\text{g}^{-1}$ . The latter are smaller than the observed dry values, which are  $8 \text{ m}^2\text{g}^{-1}$  or greater in  
26 almost all boxes. GEOS-5 underestimates it most severely in both layers.



1           The underestimates are more pronounced when humidification is taken into consideration.  
2   The aerosol swelling from moisture within the FT contributes 20% or less to the measured  
3   extinction. In contrast, UM, which provides both dry and ambient extinction, sees humidification  
4   by around 50% (compare UM Dry and UM Ambient in Fig. 16). WRF-CAM5 also has a large  
5   humidification factor, although the dry values are not shown in Fig. 16. On a dry, pre-aggregation  
6   basis (Fig. 15), the geometric mean for cases with the combined mass exceeding  $10 \mu\text{m}^{-3}$  is  $2.0$   
7    $\text{m}^2\text{g}^{-1}$  for WRF-CAM5, compared with  $8.5 \text{m}^2\text{g}^{-1}$  for the dry observation (Fig. 15g) and  $1.2 \text{m}^2\text{g}^{-1}$   
8   for GEOS-5 (Fig. 15i).

9           While the observations may have systematic biases such as underestimates in the OA  
10   masses, it is unlikely that they are large enough to explain the model-observation discrepancies in  
11   quasi-MEE. Mie calculations for common ranges of refractive index and density find that MEE  
12   for the observed UHSAS size distributions cannot be much smaller than  $4 \text{m}^2\text{g}^{-1}$ ; the quasi-MEE  
13   should be greater than this. The underestimates by some of the models are counterintuitive. With  
14   the volumetric mean diameter around 200 nm and overestimated, and with scattering Ångström  
15   exponent underestimated, the MEE and quasi-MEE are expected to be overestimated.

16           Furthermore, the pre-aggregation values of quasi-MEE (Fig. 15) in the two FT layers are  
17   less diverse with the observations (the geometric standard deviation is 1.4) than with the models  
18   (2.4 and 1.8, respectively). WRF-CAM5 evidently has three distinct values for the smoke,  
19   regardless of the day of flight. What little variations the observed relationships have depend  
20   somewhat on the flight day in a way that is not reproduced by the two models.

21           These results reveal the difficulty in representing both aerosol extinction and mass  
22   correctly. MEE serves as either the very cause of such limitation or a test of realism, depending on  
23   whether a model estimates the two aerosol properties independently from each other or not. If it  
24   does, then the model representation of aerosol mixing states, size, and refractive indexes, as well  
25   as ambient RH matters.

26           So far we have discussed the means and their biases. Our data also allow discussion of the  
27   random deviations between the models and observations, expressed by the RMSD of the box



1 means over the corridors. They are significantly greater than the magnitude of systematic biases  
2 for most extensive properties. Also, within any of the boxes there is no clear correspondence  
3 between the modeled and observed variabilities.

4 These are partly a result of counting statistics. Disagreement is found when just a few  
5 minutes of data are available for in-plume measurements in a given comparison gridbox. For  
6 example, the near-coast boxes at 8° S in the FT layers have only 4-5 minutes of data. Also, some  
7 of the observations represent a small fraction of the flight hours. For example, 4STAR provides  
8 relatively sporadic sampling of ACAOD, as the aircraft needed to be located right above clouds.

9 The variability can also be attributed to model specifications. GEOS-Chem generally  
10 exhibits greater variability, both within boxes and across them, than WRF-CAM5. This is most  
11 noticeable in ACAOD. Since these two models employ the same daily emission scheme and  
12 allocate it to diurnal cycle representative of daytime burning in similar manners, the difference in  
13 the variability must be due to other aerosol processes and model resolution.

14 For the intensive optical properties, the variability in the modeled values is typically much  
15 smaller than the observed variability. As an exception, EAM-E3SM's SSA values vary more  
16 widely than do the observations within each box in the lower FT. But they significantly  
17 overestimate the observations, possibly because of weak emissions of absorbing smoke particles  
18 in this model. SSA variability is a topic addressed in accompanying papers (Pistone et al., 2019;  
19 Doherty et al., in preparation).

## 20 **8. Summary**

21 We have compared six model representations of biomass-burning smoke and other aerosols  
22 against the 130-hour airborne observations made over the southeast Atlantic in September 2016.  
23 The major findings are:

- 24 • All six models underestimate the smoke base height. GEOS-5 and GEOS-Chem do so most  
25 severely, by 1400 m and 900 m respectively. The two models significantly overestimate  
26 the OA and BC masses, but not CO mixing ratio, in the MBL.



- 1       ● GEOS-5, EAM-E3SM, UM and WRF-CAM5 underestimate the ratio of light extinction to  
2       carbonaceous masses in 3-6 km altitude. While the OA mass is generally overestimated,  
3       extinction coefficient in the FT is biased low by some models.
- 4       ● The aerosol loads sampled in ORACLES 2016 are generally between -10% and +30% of  
5       the regional September average, according to WRF-CAM5 and GEOS-5.

6  
7



## 1     **9.     Appendix**

### 2             **9.1.     Observations**

#### 3                     **9.1.1.     SP2**

4             A Single Particle Soot Photometer (SP2) was deployed to measure the mass of individual  
5 refractory BC (rBC) particles by heating them to incandescence when passing a powerful laser  
6 beam (Schwarz et al., 2006; Stephens et al., 2003). The peak value of this incandescence signal  
7 has been shown to linearly correlate with the mass of the rBC particle (Stephens et al., 2003). The  
8 unit was calibrated for various rBC masses with Fullerene soot (Alfaa Aesar, Lot #F12S011) using  
9 Fullerene effective density estimates from Gysel et al. (2011). Assuming a density of  $1.8 \text{ g cm}^{-3}$   
10 for airborne rBC mass measurements the detection limit of the 4-channel instrument was in the  
11 range of 55-524 nm mass-equivalent diameter (MED). Overall, uncertainty of the SP2 mass  
12 measurements due to laser power and pressure fluctuations as well as detection limits has been  
13 estimated to 25% (Schwarz et al., 2006), while rBC concentration losses are expected to be small  
14 since much of the ambient BC number concentration is found within the detection limits of the  
15 SP2 (Schwarz et al., 2010).

#### 16                     **9.1.2.     AMS**

17             Bulk submicron non-refractory aerosol composition ( $\sim 50$  to  $500 \text{ nm}$  vacuum aerodynamic  
18 diameter) was provided by the Time of Flight (ToF) – Aerodyne aerosol mass spectrometer (AMS)  
19 in form of organic mass (ORG), sulfate ( $\text{SO}_4$ ), nitrate ( $\text{NO}_3$ ), and ammonium ( $\text{NH}_4$ ) (DeCarlo et  
20 al., 2008). The AMS sampled at a rate of  $\sim 1.38 \text{ cm}^3 \text{ s}^{-1}$ , and used an aerodynamic lens at constant  
21 pressure ( $600 \text{ hPa}$ ) to focus  $35 \text{ nm} - 500 \text{ nm}$  non refractory particles onto the  $600^\circ\text{C}$  heated surface  
22 under high vacuum  $\sim 10^{-5} \text{ Pa}$ . The particles are then evaporated off the heated surface, and ionized  
23 by  $70 \text{ eV}$  electron impaction. The aerosol then passes through a mechanical chopper operating at  
24  $100 - 150 \text{ Hz}$ , which alternately blocks and unblocks the particle beam. Lastly, the particles are  
25 carried through the flight chamber chemically analyzed by the Time of Flight Mass Spectrometer



1 (ToF-MS). The AMS was generally operated in the high sensitivity V-mode to facilitate constant  
2 measurements during flights. The accuracy of these measurements was estimated to 50% with 10%  
3 precision during ORACLES. A more thorough description of the University of Hawaii AMS and  
4 data processing techniques using data analysis toolkit SQUIRREL v.1.571 and PIKA v.1.161 can  
5 be found elsewhere (Shank et al., 2012; Sueper, 2018)

### 6 **9.1.3. UHSAS**

7 Particle size distributions from 60 to 1000 nm were measured with a Ultra-High Sensitivity  
8 Aerosol Spectrometer (Droplet Measurement Technologies, Boulder CO, USA). It uses scattered  
9 light from a 1054 nm laser to determine particle size. The long wavelength suppresses the  
10 ambiguity due to Mie scattering, though the highly absorbing nature of the ORACLES aerosol  
11 may result in substantial undersizing of particles > 300 nm. It was calibrated with monodisperse  
12 polystyrene latex spheres. The inlet system included a 400°C thermal denuder that could be  
13 switched in and out to identify the refractory fraction of the aerosol, though those data are not  
14 presented here. The inlet system had significant losses, particularly for particles <80nm.

### 15 **9.1.4. Nephelometer and PSAP**

16 Total and submicrometer aerosol light scattering were measured onboard the aircraft using  
17 two TSI model 3563 3- $\lambda$  nephelometers (at 450, 550, and 700 nm) corrected according to Anderson  
18 and Ogren (1998). Light absorption coefficients (at 470, 530 and 660 nm) were measured using  
19 two Radiance Research particle soot absorption photometers (PSAP's). The PSAP absorption  
20 corrections were performed according to an updated algorithm (Virkkula, 2010), however levels  
21 of instrument noise remain  $0.5 \text{ Mm}^{-1}$  for a 240–300 s sample average, comparable to values  
22 reported previously (Anderson et al., 2003; McNaughton et al., 2011). The SSA at 530 nm was  
23 calculated from the scattering and absorption measurements, after adjusting the absorption  
24 coefficients to the wavelength by linear regression on the log-log space.



### 1                    **9.1.5. High spectral resolution lidar (HSRL-2)**

2                    The NASA Langley 2<sup>nd</sup> generation airborne High Spectral Resolution Lidar (HSRL-2) was  
3                    deployed on board the ER2 and made remote-sensing measurements below the aircraft of vertically  
4                    resolved aerosol extinction coefficient (355 nm, 532 nm), aerosol backscattering coefficient (355,  
5                    532, 1064 nm) and aerosol depolarization (355, 532, 1064 nm). Other products include AOD,  
6                    AOD above cloud, lidar ratio (extinction to backscatter ratio), Ångström exponent, and a  
7                    qualitative aerosol type mask (Burton et al., 2012). AOD, extinction and backscatter are measured  
8                    using the HSRL technique (Shipley et al., 1983), which is implemented using an iodine filter at  
9                    532 nm (Hair et al., 2008) and an interferometer at 355 nm (Burton et al., 2018). Vertical  
10                    resolutions are 315 m for extinction, lidar ratio, and extinction Ångström exponent; and 15 m for  
11                    backscatter, particle depolarization ratio, and backscatter-related Ångström exponent. Horizontal  
12                    resolution is 10 seconds for backscatter and depolarization or about 2 km at a typical ER2 cruise  
13                    speed. For extinction and AOD, the horizontal resolution is one minute or about 12 km. Note that  
14                    during ORACLES 2017 and 2018 HSRL-2 was deployed from the NASA P3 aircraft. Further  
15                    details about the instrument, calibration, and uncertainty can be found in Hair et al. (2008), Rogers  
16                    et al. (2009) and Burton et al. (2018).

### 17                    **9.1.6. Airborne Sunphotometer (4STAR)**

18                    Aerosol Optical Depth (AOD) is measured from the solar direct beam's attenuation using  
19                    the Spectrometers for Sky-Scanning Sun-Tracking Atmospheric Research (4STAR) (Dunagan et  
20                    al., 2013) integrated on board the NASA P3 aircraft. Using 2 spectrometers, 4STAR samples light  
21                    with wavelengths ranging from 350 nm to 1750 nm, with sampling resolution of 0.2 - 1 nm below  
22                    1000 nm and 3 - 6 nm at longer wavelengths. The full width of the field of view for the direct  
23                    beam irradiance measurement is 2.4° with radiometric deviations of less than 1% across this span.  
24                    4STAR is calibrated pre- and post- deployment using the Langley extrapolation method at the  
25                    Mauna Loa Observatory, in addition to comparing AOD measured during high altitude flight  
26                    segments to stratospheric aerosol. The relative standard deviation of all these calibrations is 0.83%



1 (1.12%) at 500 nm (1040 nm). After calibration errors, corrections for window deposition,  
2 instability in tracking, and internal throughput variations, the average uncertainty for 4STAR  
3 during ORACLES 2016 for the AC-AOD is 0.011 (0.013) at 501 nm (1020 nm) (LeBlanc et al.,  
4 2019)

### 5 **9.1.7. Carbon monoxide**

6 CO was measured with a gas-phase CO/CO<sub>2</sub>/H<sub>2</sub>O Analyzer (ABB/Los Gatos Research  
7 CO/CO<sub>2</sub>/H<sub>2</sub>O Analyzer (907-0029)), modified for flight operations. It uses off-Axis ICOS  
8 technology to make stable cavity enhanced absorption measurements of CO, CO<sub>2</sub>, and H<sub>2</sub>O in the  
9 infrared spectral region, technology that previously flew on other airborne research platforms with  
10 a precision of 0.5 ppbv over 10 seconds (Liu et al., 2017; Provencal et al., 2005)

## 11 **9.2. Models**

12 Refer to Table 2 for a summary, including model resolution.

### 13 **9.2.1. WRF-CAM5**

14 WRF-CAM5 is a version of the WRF-Chem model that is coupled with the Community  
15 Atmosphere Model version 5 (CAM5) physics package, as implemented by (Ma et al., 2014). The  
16 CAM5 physics suite includes the deep convection scheme of Zhang and McFarlane (1995), the  
17 shallow cumulus scheme (Bretherton and Park, 2009), the University of Washington turbulence  
18 parameterization (Bretherton and Park, 2009), the Morrison and Gettelman (2008) two-moment  
19 microphysics scheme, a simplified macrophysics scheme (Neale et al., 2010), and a modal aerosol  
20 module with three modes (Aitken, Accumulation, and Coarse) (MAM3) (Liu et al., 2012) coupled  
21 with the gas phase chemistry of Carbon Bond Mechanism version Z (Zaveri and Peters, 1999). All  
22 aerosol species within each mode is assumed to be internally mixed and mass by species and total  
23 number concentrations are tracked. Aerosol optical properties are computed using the WRF-Chem  
24 routines (Fast et al., 2006) by converting MAM3 modes into eight sectional size bins (39 nm to 10  
25 μm) followed by Mie theory calculation. Organic aerosol and black carbon refractive indices are



1 assumed to be  $1.45+0i$  (e.g, no brown carbon considered) and  $1.85+0.71i$  constant across  
2 shortwave radiation. Cloud droplet activation is represented by Fountoukis and Nenes (2005) as  
3 implemented by Zhang et al. (2015) into WRF-CAM5 for giant CCN, CCN from insoluble  
4 particles such as black carbon and dust particles. The effect of convective entrainment on aerosol  
5 activation (Barahona and Nenes, 2007) is only applied to convective clouds. The Zhang and  
6 McFarlane deep convection scheme has been modified by Lim et al. (2014) following Song and  
7 Zhang (2011) to include a two-moment cloud microphysics parameterization for convective  
8 clouds. Hence aerosol effects on clouds and precipitation are represented for both convective and  
9 non-convective clouds in WRF-CAM5. Daily smoke emissions are from the Quick Fire Emission  
10 Data set version 2 (QFED2) (Darmenov and da Silva, 2013) and a diurnal cycle representative of  
11 daytime burning is applied. The model was initialized every 5 days from the NCEP Final  
12 Operational Global Analysis (FNL) on a 1 by 1 degree grid, and CAMS reanalysis, with the first  
13 3 days of simulations considered as model spin-up and not used in our analysis.

### 14 **9.2.2. GEOS-5**

15 The Goddard Earth Observing System version 5, is a global modeling system developed at  
16 NASA Global Modeling and Assimilation Office (GMAO)(Molod et al., 2015; Rienecker et al.,  
17 2008). It is a state-of-art modeling tool used for near-real time weather and air quality forecasts. It  
18 also serves as tool for climate variability studies and reanalysis for research (MERRA-2)(Randles  
19 et al., 2017). GEOS-5 includes modules for solving atmospheric circulation and composition,  
20 chemistry, ocean circulation and land surface processes. Furthermore, GEOS-5 uses a robust  
21 atmospheric data assimilation system using the Grid-point Statistical Interpolation (GSI)  
22 algorithm, which includes AOD assimilation from MODIS (Terra and Aqua), among others.  
23 Aerosols are treated online using GOCART (Goddard Chemistry Aerosol Radiation and  
24 Transport) (Chin et al., 2002; Colarco et al., 2010). Black and organic carbon aerosols are treated  
25 separately, with organic carbon aerosols represented as a function of the particulate organic matter  
26 (POM), with  $POM = 1.4 * \text{organic carbon mass}$  (Textor et al., 2006). The single-moment mass is



1 converted to an extinction using a black carbon mass extinction efficiency of  $10.7 \text{ m}^2\text{g}^{-1}$  and  $5.83$   
2  $\text{m}^2\text{g}^{-1}$  for POM, both at 550 nm (Colarco et al., 2010). The carbonaceous aerosols are coupled with  
3 the radiation module. QFED2 is used as daily input of biomass burning emissions. For this study,  
4 GEOS-5 used initial conditions from its reanalysis product (MERRA-2), with a resolution of  
5 around 25 km ( $0.25^\circ \times 0.31^\circ$  latitude x longitude grid) with 72 vertical levels (hybrid-sigma) from  
6 the surface

### 7 **9.2.3. GEOS-Chem**

8 GEOS-Chem version 12.0.0 (<http://www.geos-chem.org/>) is a global 3-D model of  
9 atmospheric composition driven by assimilated meteorological data GEOS-FP data (Lucchesi,  
10 2013) from the Global Modeling and Assimilation Office (GMAO) at NASA Goddard Space  
11 Flight Center. The GEOS-FP data have 1-hourly and 3-hourly temporal resolution, 72 vertical  
12 layers, and  $0.25^\circ \times 0.3125^\circ$  horizontal resolution. The original horizontal resolution is then degraded  
13 to  $2^\circ \times 2.5^\circ$  for the input to GEOS-Chem. Aerosol types simulated in GEOS-Chem include sulfate–  
14 nitrate–ammonium aerosols, carbonaceous aerosols, sea salt, and mineral dust. The simulation of  
15 carbonaceous aerosols was originally described by Park et al. (2003). Daily smoke emissions have  
16 been updated to the Quick Fire Emission Data set version 2 (QFED2) (Darmenov and da Silva,  
17 2015) and a diurnal cycle representative of daytime burning is applied. Dry deposition in GEOS-  
18 Chem follows a stand resistance-in-series scheme (Wesely, 1989), accounting for gravitational  
19 settling and turbulent dry transfer of particles to the surface (Zhang et al., 2001). Wet deposition  
20 in GEOS-Chem includes scavenging in convective updrafts, as well as in-cloud and below-cloud  
21 scavenging from convective and large-scale precipitation (Liu et al., 2001), and distinguish the  
22 difference between snow/ice scavenging and rain scavenging (Wang et al., 2011, 2014). Aerosol  
23 optical depth are calculated online using Mie theory, assuming lognormal distribution of externally  
24 mixed aerosols after accounting for hygroscopic growth. The optical properties used in the  
25 calculation are based on the Global Aerosol Data Set (GADS) data (Koepke et al., 1997), with

1 modifications in size distribution (Drury et al., 2010; Jaeglé et al., 2011; Wang, 2003a, 2003b),  
2 and hygroscopic growth factors (Jimenez et al., 2009).

### 3 **9.2.4. EAM-E3SM**

4 The EAM-E3SM is the atmospheric component of the Department of Energy Exascale  
5 Energy Earth System Model (E3SM) version 1 (Golaz et al., 2019). It is a global atmospheric  
6 model branched off from the CAM 5.3 and updated with the physics similar to changes from  
7 CAM5.3 to CAM6 incorporated. The model configuration used in this study includes a spectral  
8 element dynamical core at approximately 100 km horizontal resolution and 72 vertical layers. The  
9 planetary boundary layer turbulence, shallow convection and cloud macrophysics are treated with  
10 a simplified version of the unified parameterization - CLUBB (Cloud Layers Unified By  
11 Binormals; Larson and Golaz (2005); Larson (2017)). The EAM-E3SM aerosol module is the four-  
12 mode version of the Modal Aerosol Module (MAM4) in the CAM5.3 (Liu et al., 2016). It simulates  
13 internally mixed major aerosol compounds (sulfate, BC, primary and secondary organic matter,  
14 dust, sea salt and marine organic aerosols), which are distributed into three size modes including  
15 Aitken, accumulation, and coarse modes, plus an additional primary carbon mode representing  
16 freshly emitted BC and primary organic matter. In each aerosol size mode, mass concentrations of  
17 aerosol compounds and a total number concentration of aerosol mixture are calculated at each  
18 model time step and evolve in time. Detailed description of EAM physics and model evaluations  
19 are given in Rasch et al. (2019) and Xie et al. (2018). For this study, EAM simulations were  
20 conducted in the nudging mode with temperature, wind speeds and moisture fields nudged to the  
21 ERA-Interim reanalysis data every 6 hours. One-year model simulations are performed after  
22 spinning-up the model and model outputs from August to October are used in comparison. Aerosol  
23 and cloud properties are output every 3 hours to account for the diurnal variations. Emissions of  
24 anthropogenic aerosols are taken from the IPCC-AR5 emissions for circ. year 2000. Biomass  
25 burning emissions are based on GFED emissions averaged over 1997 and 2000.



### 1                    **9.2.5. Unified Model**

2                    The Unified Model is the numerical weather prediction and global climate model of the  
3 UK Meteorological Office, known also as HadGEM3 in its climate modeling configuration. The  
4 model configuration used here is similar to the global model setup used by Gordon et al. (2018),  
5 but is now based on GA7.1 with version 11.2 of the model code, while Gordon et al. (2018) used  
6 a setup based on GA6.1 with version 10.3. The spatial resolution is N216 (approximately 60x90km  
7 at the Equator) and for this study instantaneous diagnostic output at three-hourly intervals was  
8 produced. The model sea surface temperatures are fixed from the OSTIA temperature record and  
9 the horizontal winds above the boundary layer are nudged to ERA-interim reanalysis. The model  
10 run is a continuation of that used for 1-10 August 2016 by Gordon et al. (2018), which was  
11 initialized from an operational forecast on 20 July 2016. Aerosols in the model are simulated using  
12 the two-moment GLOMAP-mode scheme within the United Kingdom Chemistry and Aerosols  
13 framework. There are five log-normal aerosol modes containing sulfate, black and organic carbon,  
14 and sea salt components; dust and nitrate are not included. A reduced chemistry scheme for aerosol  
15 formation via the sulfur cycle uses oxidants from climatologies. Smoke emissions are read in daily  
16 from the FEER inventory for 2016 (Ichoku and Ellison, 2014) as a log-normal mode of aerosol  
17 with diameter 120nm; they are distributed vertically within the boundary layer as in Gordon et al.  
18 (2018). Other emissions are either calculated by the model, as in the case of sea spray, or taken  
19 from the CMIP5 inventories. The single-moment cloud microphysics scheme of Wilson and  
20 Ballard (1999) and pc2 sub-grid cloud scheme of Wilson et al (2008) are used. Convection is  
21 parameterized where it cannot be resolved. The refractive index of BC and the updraft speeds in  
22 the activation scheme now follow GA7.1 prescriptions used in the CMIP6 experiments, while the  
23 hygroscopicity of the aerosol constituent components now follows Petters and Kreidenweis  
24 (2007), which is another change compared to Gordon et al. (2018).



### 1                    9.2.6.    ALADIN-Climate

2                    The ALADIN-Climate model is a regional climate model (RCM), which is developed in  
3                    CNRM/Meteo-France. We use here the version 6 of ALADIN-Climate (Mallet et al., 2019), which  
4                    has a similar physical package to the global climate model ARPEGE-Climate (Voldoire et al.,  
5                    2017) used in the CMIP6 exercise. It is a bi-spectral semi-implicit semi-lagrangian model, with a  
6                    12 km horizontal resolution. ALADIN-Climate includes the Fouquart and Morcrette radiation  
7                    scheme (Morcrette, 1989), based on the ECMWF model incorporating effects of greenhouse gases,  
8                    direct and semi-direct effects of aerosols as well as the first indirect effect of hydrophilic aerosols.  
9                    The ALADIN-Climate model incorporates a radiative scheme to take into account the direct and  
10                   semi-direct effects of five aerosol types (sea salt, desert dust, sulfates, black and organic carbon  
11                   aerosols). Here, a new version of the ALADIN-Climate model, including notably a more detailed  
12                   treatment (optical and hygroscopic properties, e-folding time) of smoke aerosols, have been used  
13                   for this specific inter-comparison exercise (Mallet et al., 2019). The ALADIN-Climate simulation  
14                   has been conducted for three months (August-September-October 2016) englobing the ORACLES  
15                   period. The model used the ERA-INT reanalyses as lateral boundary conditions. For this  
16                   simulation, the GFED emissions inventory based on CMIP6 has been used for biomass burning  
17                   emissions, with scale factors from Petrenko et al. (2017). An important point is that aerosol (SO<sub>2</sub>,  
18                   BC and OC) emissions for the year 2014 have been used as this specific year represents the last  
19                   year of the historical CMIP6 period using realistic BC-OC emissions from biomass-burning (based  
20                   on GFED inventory). Emissions have been used as the first model level without any considerations  
21                   about the altitude of injection of smoke particles in this simulation. As detailed in Mallet et al.  
22                   (2019), this model does not integrate secondary organics and a POM to OC ratio have been used  
23                   in this simulation, based on Formenti et al. (2003).



## 1 **Data availability**

2 The P3 and ER2 observational data (NASA Ames Earth Science Project Office, 2017a,  
3 2017b) are available through [www.espo.nasa.gov/oracles](http://www.espo.nasa.gov/oracles). The aggregated model and observation  
4 products are available at  
5 [https://espo.nasa.gov/sites/default/files/box\\_P3ER2Models\\_2016mmdd\\_R8.nc](https://espo.nasa.gov/sites/default/files/box_P3ER2Models_2016mmdd_R8.nc) .  
6

## 7 **Author contribution**

8 SPB, RF, AD, SF, SGH, SL, CF, MSR, KP, JRP, EJS, JRB and YS operated instruments  
9 during the ORACLES intensive observation periods. PES, GAF, HG, KL, MM, YF, QW, YC,  
10 GRC, AdS, RG, RL, YZ delivered model products. LP and JMR developed the methodology of  
11 determining MBL height. PES, SJD, JR, RW and PZ formulated the model-observation  
12 comparison. YS organized all products and applied statistical techniques. YS, GAF and PZ  
13 visualized the results. YS, PZ, PES wrote most of the first draft. YS, PES, GAF, SPB, RF, SJD,  
14 HG, MM, YF, SL, MSR, KP, RL, YZ, LP, RW and PZ edited the manuscript. JR, RW and PZ led  
15 the efforts to acquire funding for the ORACLES mission. PZ administered and supervised the  
16 study.

## 17 **Competing Interests**

18 The authors declare that they have no conflict of interest.

## 19 **Acknowledgements**

20 ORACLES is a NASA Earth Venture Suborbital 2 investigation, funded by NASA's Earth  
21 Science Division and managed through the Earth System Science Pathfinder Program Office. HG



1 is funded by the NERC CLARIFY project under grant NE/L013479/1, and acknowledges use of  
2 the Monsoon2 system, a collaborative facility supplied under the Joint Weather and Climate  
3 Research Programme, a strategic partnership between the UK Met Office and the Natural  
4 Environment Research Council. YZ was supported by the U.S. Department of Energy Office of  
5 Science Biological and Environmental Research as part of the Global and Regional Climate  
6 Modeling programs (DE-SC0006695). WRF-CAM5 was developed with the high-performance  
7 computing support from Kraken and Stampede, provided as an Extreme Science and Engineering  
8 Discovery Environment (XSEDE) digital service by the Texas Advanced Computing Center  
9 (TACC) (<http://www.tacc.utexas.edu>), which is supported by National Science Foundation grant  
10 number ACI-1053575., and the National Energy Research Scientific Computing Center (NERSC),  
11 which is supported by the Office of Science of the U.S. Department of Energy under Contract No.  
12 DE-AC02-05CH11231. The authors would like to thank Sampa Das for her valuable comments,  
13 and Nicolas Bellouin for the code to diagnose dry aerosol optical properties from the Unified  
14 Model.

## 15 **References**

- 16 Adebisi, A. A. and Zuidema, P.: Low Cloud Cover Sensitivity to Biomass-Burning Aerosols and  
17 Meteorology over the Southeast Atlantic, *J. Clim.*, 31(11), 4329–4346, 2018.
- 18 Adebisi, A. A., Zuidema, P. and Abel, S. J.: The Convolution of Dynamics and Moisture with the  
19 Presence of Shortwave Absorbing Aerosols over the Southeast Atlantic, *J. Clim.*, 28(5), 1997–2024,  
20 2015.
- 21 Anderson, T. L. and Ogren, J. A.: Determining aerosol radiative properties using the TSI 3563 integrating  
22 nephelometer, *Aerosol Sci. Technol.*, 29, 57–69, 1998.
- 23 Anderson, T. L., Masonis, S. J., Covert, D. S., Ahlquist, N. C., Howell, S. G., Clarke, A. D. and  
24 McNaughton, C. S.: Variability of aerosol optical properties derived from in situ aircraft measurements  
25 during ACE-Asia, *J. Geophys. Res.*, 108(D23), 8647, doi:10.1029/2002JD003247, 2003.
- 26 Barahona, D. and Nenes, A.: Parameterization of cloud droplet formation in large-scale models: Including  
27 effects of entrainment, *J. Geophys. Res.*, 112(D16), 6837, 2007.



- 1 Bretherton, C. S. and Park, S.: A New Moist Turbulence Parameterization in the Community Atmosphere  
2 Model, *J. Clim.*, 22(12), 3422–3448, 2009.
- 3 Burton, S. P., Ferrare, R. A., Hostetler, C. A., Hair, J. W., Rogers, R. R., Obland, M. D., Butler, C. F.,  
4 Cook, A. L., Harper, D. B. and Froyd, K. D.: Aerosol classification using airborne High Spectral  
5 Resolution Lidar measurements – methodology and examples, *Atmospheric Measurement Techniques*,  
6 5(1), 73–98, 2012.
- 7 Burton, S. P., Hostetler, C. A., Cook, A. L., Hair, J. W., Seaman, S. T., Scola, S., Harper, D. B., Smith, J.  
8 A., Fenn, M. A., Ferrare, R. A., Saide, P. E., Chemyakin, E. V. and Müller, D.: Calibration of a high  
9 spectral resolution lidar using a Michelson interferometer, with data examples from ORACLES, *Appl.*  
10 *Opt.*, 57(21), 6061–6075, 2018.
- 11 Chand, D., Wood, R., Anderson, T. L., Satheesh, S. K. and Charlson, R. J.: Satellite-derived direct  
12 radiative effect of aerosols dependent on cloud cover, *Nat. Geosci.*, 2, 181, 2009.
- 13 Chin, M., Ginoux, P., Kinne, S., Torres, O., Holben, B. N., Duncan, B. N., Martin, R. V., Logan, J. A.,  
14 Higurashi, A. and Nakajima, T.: Tropospheric Aerosol Optical Thickness from the GOCART Model and  
15 Comparisons with Satellite and Sun Photometer Measurements, *J. Atmos. Sci.*, 59(3), 461–483, 2002.
- 16 Colarco, P., da Silva, A., Chin, M. and Diehl, T.: Online simulations of global aerosol distributions in the  
17 NASA GEOS-4 model and comparisons to satellite and ground-based aerosol optical depth, *J. Geophys.*  
18 *Res.*, 115(D14), doi:10.1029/2009jd012820, 2010.
- 19 Darmenov, A. and da Silva, A.: The Quick Fire Emissions Dataset (QFED) – Documentation of versions  
20 2.1, 2.2 and 2.4. NASA Technical Report Series on Global Modeling and Data Assimilation, NASA TM-  
21 2013-104606, 32, 183, 2013.
- 22 Darmenov, A. S. and da Silva, A. M.: The Quick Fire Emissions Dataset (QFED): Documentation of  
23 Versions 2.1, 2.2 and 2.4. Volume 38; Technical Report Series on Global Modeling and Data  
24 Assimilation, [online] Available from: <https://ntrs.nasa.gov/search.jsp?R=20180005253> (Accessed 9 May  
25 2019), 2015.
- 26 Das, S., Harshvardhan, H., Bian, H., Chin, M., Curci, G., Protonotariou, A. P., Mielonen, T., Zhang, K.,  
27 Wang, H. and Liu, X.: Biomass burning aerosol transport and vertical distribution over the South African-  
28 Atlantic region: Aerosol Transport Over SE Atlantic, *J. Geophys. Res. D: Atmos.*, 122(12), 6391–6415,  
29 2017.
- 30 DeCarlo, P. F., Dunlea, E. J., Kimmel, J. R., Aiken, A. C., Sueper, D., Crouse, J., Wennberg, P. O.,  
31 Emmons, L., Shinzuka, Y., Clarke, A., Zhou, J., Tomlinson, J., Collins, D. R., Knapp, D., Weinheimer,  
32 A. J., Montzka, D. D., Campos, T. and Jimenez, J. L.: Fast airborne aerosol size and chemistry  
33 measurements above Mexico City and Central Mexico during the MILAGRO campaign, *Atmos. Chem.*  
34 *Phys.*, 8(14), 4027–4048, 2008.
- 35 Diamond, M. S., Dobracki, A., Freitag, S., Small Griswold, J. D., Heikkila, A., Howell, S. G., Kacarab,



- 1 M. E., Podolske, J. R., Saide, P. E. and Wood, R.: Time-dependent entrainment of smoke presents an  
2 observational challenge for assessing aerosol–cloud interactions over the southeast Atlantic Ocean,  
3 *Atmos. Chem. Phys.*, 18(19), 14623–14636, 2018.
- 4 Doherty, S. J., Saide, P., Zuidema, P., Shinozuka, Y., Ferrada, G., Mallet, M., Meyer, K., Painemal, D.,  
5 Howell, S. G., Freitag, S., Smirnow, N., Dobracki, A., Podolske, J., Pfister, L., Ueyama, R., Nabat, P.,  
6 Wood, R. and Redemann, J.: A summary and model-observation comparison of vertically-resolved  
7 aerosol and cloud properties over the Southeast Atlantic, in preparation.
- 8 Drury, E., Jacob, D. J., Spurr, R. J. D., Wang, J., Shinozuka, Y., Anderson, B. E., Clarke, A. D., Dibb, J.,  
9 McNaughton, C. and Weber, R.: Synthesis of satellite (MODIS), aircraft (ICARTT), and surface  
10 (IMPROVE, EPA-AQS, AERONET) aerosol observations over eastern North America to improve  
11 MODIS aerosol retrievals and constrain surface aerosol concentrations and sources, *J. Geophys. Res. D:*  
12 *Atmos.*, 115(D14) [online] Available from:  
13 <https://rmets.onlinelibrary.wiley.com/doi/pdf/10.1029/2009JD012629>, 2010.
- 14 Dunagan, S. E., Johnson, R., Zavaleta, J., Russell, P. B., Schmid, B., Flynn, C., Redemann, J., Shinozuka,  
15 Y., Livingston, J. and Segal-Rosenhaimer, M.: Spectrometer for Sky-Scanning Sun-Tracking  
16 Atmospheric Research (4STAR): Instrument Technology, *Remote Sensing*, 5(8), 3872–3895, 2013.
- 17 Fast, J. D., Gustafson, W. I., Jr., Easter, R. C., Zaveri, R. A., Barnard, J. C., Chapman, E. G., Grell, G. A.  
18 and Peckham, S. E.: Evolution of ozone, particulates, and aerosol direct radiative forcing in the vicinity of  
19 Houston using a fully coupled meteorology-chemistry-aerosol model, *J. Geophys. Res.*, 111(D21), 2981,  
20 2006.
- 21 Fishman, J., Fakhruzzaman, K., Cros, B. and Nganga, D.: Identification of widespread pollution in the  
22 southern hemisphere deduced from satellite analyses, *Science*, 252(5013), 1693–1696, 1991.
- 23 Formenti, P., Elbert, W., Maenhaut, W., Haywood, J., Osborne, S. and Andreae, M. O.: Inorganic and  
24 carbonaceous aerosols during the Southern African Regional Science Initiative (SAFARI 2000)  
25 experiment: Chemical characteristics, physical properties, and emission data for smoke from African  
26 biomass burning, *J. Geophys. Res. D: Atmos.*, 108(D13) [online] Available from:  
27 <https://onlinelibrary.wiley.com/doi/abs/10.1029/2002JD002408>, 2003.
- 28 Fornacca, D., Ren, G. and Xiao, W.: Performance of Three MODIS Fire Products (MCD45A1,  
29 MCD64A1, MCD14ML), and ESA Fire\_CCI in a Mountainous Area of Northwest Yunnan, China,  
30 *Characterized by Frequent Small Fires*, *Remote Sensing*, 9(11), 1131, 2017.
- 31 Fountoukis, C. and Nenes, A.: Continued development of a cloud droplet formation parameterization for  
32 global climate models, *J. Geophys. Res.*, 110(D11), doi:10.1029/2004jd005591, 2005.
- 33 Golaz, J., Caldwell, P. M., Van Roekel, L. P., Petersen, M. R., Tang, Q., Wolfe, J. D., Abeshu, G.,  
34 Anantharaj, V., Asay-Davis, X. S., Bader, D. C., Baldwin, S. A., Bisht, G., Bogenschutz, P. A.,  
35 Branstetter, M., Brunke, M. A., Brus, S. R., Burrows, S. M., Cameron-Smith, P. J., Donahue, A. S.,  
36 Deakin, M., Easter, R. C., Evans, K. J., Feng, Y., Flanner, M., Foucar, J. G., Fyke, J. G., Griffin, B. M.,



- 1 Hannay, C., Harrop, B. E., Hoffman, M. J., Hunke, E. C., Jacob, R. L., Jacobsen, D. W., Jeffery, N.,  
2 Jones, P. W., Keen, N. D., Klein, S. A., Larson, V. E., Leung, L. R., Li, H., Lin, W., Lipscomb, W. H.,  
3 Ma, P., Mahajan, S., Maltrud, M. E., Mamejtanov, A., McClean, J. L., McCoy, R. B., Neale, R. B., Price,  
4 S. F., Qian, Y., Rasch, P. J., Reeves Eyre, J. E. J., Riley, W. J., Ringler, T. D., Roberts, A. F., Roesler, E.  
5 L., Salinger, A. G., Shaheen, Z., Shi, X., Singh, B., Tang, J., Taylor, M. A., Thornton, P. E., Turner, A.  
6 K., Veneziani, M., Wan, H., Wang, H., Wang, S., Williams, D. N., Wolfram, P. J., Worley, P. H., Xie, S.,  
7 Yang, Y., Yoon, J., Zelinka, M. D., Zender, C. S., Zeng, X., Zhang, C., Zhang, K., Zhang, Y., Zheng, X.,  
8 Zhou, T. and Zhu, Q.: The DOE E3SM Coupled Model Version 1: Overview and Evaluation at Standard  
9 Resolution, *J. Adv. Model. Earth Syst.*, 108, 1, 2019.
- 10 Gordon, H., Field, P. R., Abel, S. J., Dalvi, M., Grosvenor, D. P., Hill, A. A., Johnson, B. T.,  
11 Miltenberger, A. K., Yoshioka, M. and Carslaw, K. S.: Large simulated radiative effects of smoke in the  
12 south-east Atlantic, *Atmos. Chem. Phys.*, 18(20), 15261–15289, 2018.
- 13 de Graaf, M., Bellouin, N., Tilstra, L. G., Haywood, J. and Stammes, P.: Aerosol direct radiative effect of  
14 smoke over clouds over the southeast Atlantic Ocean from 2006 to 2009: DE GRAAF ET AL, *Geophys.*  
15 *Res. Lett.*, 41(21), 7723–7730, 2014.
- 16 Gysel, M., Laborde, M., Olfert, J. S., Subramanian, R. and Gröhn, A. J.: Effective density of Aquadag  
17 and fullerene soot black carbon reference materials used for SP2 calibration, *Atmospheric Measurement*  
18 *Techniques*, 4(12), 2851–2858, 2011.
- 19 Hair, J. W., Hostetler, C. A., Cook, A. L., Harper, D. B., Ferrare, R. A., Mack, T. L., Welch, W.,  
20 Izquierdo, L. R. and Hovis, F. E.: Airborne High Spectral Resolution Lidar for profiling aerosol optical  
21 properties, *Appl. Opt.*, 47(36), 6734–6752, 2008.
- 22 Ichoku, C. and Ellison, L.: Global top-down smoke-aerosol emissions estimation using satellite fire  
23 radiative power measurements, *Atmos. Chem. Phys.*, 14(13), 6643–6667, 2014.
- 24 Jaeglé, L., Quinn, P. K., Bates, T. S., Alexander, B. and Lin, J.-T.: Global distribution of sea salt aerosols:  
25 new constraints from in situ and remote sensing observations, , doi:10.5194/acp-11-3137-2011, 2011.
- 26 Jimenez, J. L., Canagaratna, M. R., Donahue, N. M., Prevot, A. S. H., Zhang, Q., Kroll, J. H., DeCarlo, P.  
27 F., Allan, J. D., Coe, H., Ng, N. L., Aiken, A. C., Docherty, K. S., Ulbrich, I. M., Grieshop, A. P.,  
28 Robinson, A. L., Duplissy, J., Smith, J. D., Wilson, K. R., Lanz, V. A., Hueglin, C., Sun, Y. L., Tian, J.,  
29 Laaksonen, A., Raatikainen, T., Rautiainen, J., Vaattovaara, P., Ehn, M., Kulmala, M., Tomlinson, J. M.,  
30 Collins, D. R., Cubison, M. J., Dunlea, E. J., Huffman, J. A., Onasch, T. B., Alfarra, M. R., Williams, P.  
31 I., Bower, K., Kondo, Y., Schneider, J., Drewnick, F., Borrmann, S., Weimer, S., Demerjian, K., Salcedo,  
32 D., Cottrell, L., Griffin, R., Takami, A., Miyoshi, T., Hatakeyama, S., Shimono, A., Sun, J. Y., Zhang, Y.  
33 M., Dzepina, K., Kimmel, J. R., Sueper, D., Jayne, J. T., Herndon, S. C., Trimborn, A. M., Williams, L.  
34 R., Wood, E. C., Middlebrook, A. M., Kolb, C. E., Baltensperger, U. and Worsnop, D. R.: Evolution of  
35 organic aerosols in the atmosphere, *Science*, 326(5959), 1525–1529, 2009.
- 36 Kacenelenbogen, M., Vaughan, M. A., Redemann, J., Hoff, R. M., Rogers, R. R., Ferrare, R. A., Russell,  
37 P. B., Hostetler, C. A., Hair, J. W. and Holben, B. N.: An accuracy assessment of the CALIOP/CALIPSO



- 1 version 2/version 3 daytime aerosol extinction product based on a detailed multi-sensor, multi-platform  
2 case study, *Atmos. Chem. Phys.*, 11(8), 3981–4000, 2011.
- 3 Katich, J. M., Samset, B. H., Bui, T. P., Dollner, M., Froyd, K. D., Campuzano-Jost, P., Nault, B. A.,  
4 Schroder, J. C., Weinzierl, B. and Schwarz, J. P.: Strong Contrast in Remote Black Carbon Aerosol  
5 Loadings Between the Atlantic and Pacific Basins, *J. Geophys. Res. D: Atmos.*, 123(23), 13,386–13,395,  
6 2018.
- 7 Klein, S. A. and Hartmann, D. L.: The Seasonal Cycle of Low Stratiform Clouds, *J. Clim.*, 6, 1587–1606,  
8 1993.
- 9 Koch, D., Schulz, M., Kinne, S., McNaughton, C., Spackman, J. R., Balkanski, Y., Bauer, S., Berntsen,  
10 T., Bond, T. C., Boucher, O., Chin, M., Clarke, A., Luca, N. D., Dentener, F., Diehl, T., Dubovik, O.,  
11 Easter, R., Fahey, D. W., Feichter, J., Fillmore, D., Freitag, S., Ghan, S., Ginoux, P., Gong, S., Horowitz,  
12 L., Iversen, T., Kirkevåg, A., Klimont, Z., Kondo, Y., Krol, M., Liu, X., Miller, R., Montanaro, V.,  
13 Moteki, N., Myhre, G., Penner, J. E., Perlwitz, J., Pitari, G., Reddy, S., Sahu, L., Sakamoto, H., Schuster,  
14 G., Schwarz, J. P., Seland, Ø., Stier, P., Takegawa, N., Takemura, T., Textor, C., van Aardenne, J. A. and  
15 Zhao, Y.: Evaluation of black carbon estimations in global aerosol models, *Atmos. Chem. Phys.*, 9(22),  
16 9001–9026, 2009.
- 17 Koepke, P., Hess, M., Schult, I. and Shettle, E.: Global Aerosol Data Set, Rep. 243, Max Planck Institute  
18 for Meteorology, 1997.
- 19 Larson, V. E.: CLUBB-SILHS: A parameterization of subgrid variability in the atmosphere, arXiv  
20 [physics.ao-ph] [online] Available from: <http://arxiv.org/abs/1711.03675>, 2017.
- 21 Larson, V. E. and Golaz, J.-C.: Using Probability Density Functions to Derive Consistent Closure  
22 Relationships among Higher-Order Moments, *Monthly Weather Review*, 133(4), 1023–1042,  
23 doi:10.1175/mwr2902.1, 2005.
- 24 LeBlanc, S. E., Redemann, J., Flynn, C., Pistone, K., Kacenenbogen, M., Segal-Rosenheimer, M.,  
25 Shinozuka, Y., Dunagan, S., Dahlgren, R. P., Meyer, K., Podolske, J., Howell, S. G., Freitag, S., Small-  
26 Griswold, J., Holben, B., Diamond, M., Formenti, P., Piketh, S., Maggs-Kölling, G., Gerber, M. and  
27 Namwoonde, A.: Above Cloud Aerosol Optical Depth from airborne observations in the South-East  
28 Atlantic, , doi:10.5194/acp-2019-43, 2019.
- 29 Lim, K.-S. S., Fan, J., Leung, L. R., Ma, P.-L., Singh, B., Zhao, C., Zhang, Y., Zhang, G. and Song, X.:  
30 Investigation of aerosol indirect effects using a cumulus microphysics parameterization in a regional  
31 climate model: INVESTIGATION OF AIE ON REGIONAL CLIMATE, *J. Geophys. Res. D: Atmos.*,  
32 119(2), 906–926, 2014.
- 33 Liu, H., Jacob, D. J., Bey, I. and Yantosca, R. M.: Constraints from  $^{210}\text{Pb}$  and  $^7\text{Be}$  on wet deposition and  
34 transport in a global three-dimensional chemical tracer model driven by assimilated meteorological fields,  
35 *Journal of Geophysical Research: Atmospheres*, 106(D11), 12109–12128, doi:10.1029/2000jd900839,  
36 2001.



- 1 Liu, X., Easter, R. C., Ghan, S. J., Zaveri, R., Rasch, P., Shi, X., -F. Lamarque, J., Gettelman, A.,  
2 Morrison, H., Vitt, F., Conley, A., Park, S., Neale, R., Hannay, C., Ekman, A. M. L., Hess, P., Mahowald,  
3 N., Collins, W., Iacono, M. J., Bretherton, C. S., Flanner, M. G. and Mitchell, D.: Toward a Minimal  
4 Representation of Aerosols in Climate Models: Description and Evaluation in the Community  
5 Atmosphere Model CAM5, *Geoscientific Model Development*, 5(3), 709, 2012.
- 6 Liu, X., Ma, P.-L., Wang, H., Tilmes, S., Singh, B., Easter, R. C., Ghan, S. J. and Rasch, P. J.:  
7 Description and evaluation of a new four-mode version of the Modal Aerosol Module (MAM4) within  
8 version 5.3 of the Community Atmosphere Model, *Geoscientific Model Development (Online)*, 9(PNNL-  
9 SA-110649) [online] Available from: <https://www.osti.gov/biblio/1243191>, 2016.
- 10 Liu, X., Huey, L. G., Yokelson, R. J., Selimovic, V., Simpson, I. J., Müller, M., Jimenez, J. L.,  
11 Campuzano-Jost, P., Beyersdorf, A. J., Blake, D. R., Butterfield, Z., Choi, Y., Crounse, J. D., Day, D. A.,  
12 Diskin, G. S., Dubey, M. K., Fortner, E., Hanisco, T. F., Hu, W., King, L. E., Kleinman, L., Meinardi, S.,  
13 Mikoviny, T., Onasch, T. B., Palm, B. B., Peischl, J., Pollack, I. B., Ryerson, T. B., Sachse, G. W.,  
14 Sedlacek, A. J., Shilling, J. E., Springston, S., St. Clair, J. M., Tanner, D. J., Teng, A. P., Wennberg, P.  
15 O., Wisthaler, A. and Wolfe, G. M.: Airborne measurements of western U.S. wildfire emissions:  
16 Comparison with prescribed burning and air quality implications, *J. Geophys. Res. D: Atmos.*, 122(11),  
17 6108–6129, 2017.
- 18 Liu, Z., Winker, D., Omar, A., Vaughan, M., Kar, J., Treppe, C., Hu, Y. and Schuster, G.: Evaluation of  
19 CALIOP 532 nm aerosol optical depth over opaque water clouds, *Atmos. Chem. Phys.*, 15(3), 1265–  
20 1288, 2015.
- 21 Lock, A. P., Brown, A. R., Bush, M. R., Martin, G. M. and Smith, R. N. B.: A New Boundary Layer  
22 Mixing Scheme. Part I: Scheme Description and Single-Column Model Tests, *Mon. Weather Rev.*,  
23 128(9), 3187–3199, 2000.
- 24 Lucchesi, R.: File Specification for GEOS-5 FP-IT (Forward Processing for Instrument Teams), [online]  
25 Available from: <https://ntrs.nasa.gov/search.jsp?R=20150001438> (Accessed 11 April 2019), 2013.
- 26 Lu, Z., Liu, X., Zhang, Z., Zhao, C., Meyer, K., Rajapakshe, C., Wu, C., Yang, Z. and Penner, J. E.:  
27 Biomass smoke from southern Africa can significantly enhance the brightness of stratocumulus over the  
28 southeastern Atlantic Ocean, *Proc. Natl. Acad. Sci. U. S. A.*, 115(12), 2924–2929, 2018.
- 29 Mallet, M., Nabat, P., Zuidema, P., Redemann, J., Sayer, A. M., Stengel, M., Schmidt, S., Cochrane, S.,  
30 Burton, S., Ferrare, R., Meyer, K., Saide, P., Jethva, H., Torres, O., Wood, R., Saint Martin, D., Roehrig,  
31 R., Hsu, C. and Formenti, P.: Simulation of the transport, vertical distribution, optical properties and  
32 radiative impact of smoke aerosols with the ALADIN regional climate model during the ORACLES-2016  
33 and LASIC experiments, *Atmos. Chem. Phys.*, 19(7), 4963–4990, 2019.
- 34 Ma, P.-L., Rasch, P. J., Fast, J. D., Easter, R. C., Gustafson, W. I., Jr., Liu, X., Ghan, S. J. and Singh, B.:  
35 Assessing the CAM5 physics suite in the WRF-Chem model: implementation, resolution sensitivity, and  
36 a first evaluation for a regional case study, *Geoscientific Model Development*, 7(3), 755–778, 2014.



- 1 McNaughton, C. S., Clarke, A. D., Freitag, S., Kapustin, V. N., Kondo, Y., Moteki, N., Sahu, L.,  
2 Takegawa, N., Schwarz, J. P., Spackman, J. R., Watts, L., Diskin, G., Podolske, J., Holloway, J. S.,  
3 Wisthaler, A., Mikoviny, T., de Gouw, J., Warneke, C., Jimenez, J., Cubison, M., Howell, S. G.,  
4 Middlebrook, A., Bahreini, R., Anderson, B. E., Winstead, E., Thornhill, K. L., Lack, D., Cozic, J. and  
5 Brock, C. A.: Absorbing aerosol in the troposphere of the Western Arctic during the 2008  
6 ARCTAS/ARCPAC airborne field campaigns, *Atmos. Chem. Phys.*, 11(15), 7561–7582, 2011.
- 7 Molod, A., Takacs, L., Suarez, M. and Bacmeister, J.: Development of the GEOS-5 atmospheric general  
8 circulation model: evolution from MERRA to MERRA2, *Geoscientific Model Development*, 8(5), 1339–  
9 1356, 2015.
- 10 Morcrette, J.-J.: Description of the radiation scheme in the ECMWF model, , doi:10.21957/I1KILJZZE,  
11 1989.
- 12 Morrison, H. and Gettelman, A.: A New Two-Moment Bulk Stratiform Cloud Microphysics Scheme in  
13 the Community Atmosphere Model, Version 3 (CAM3). Part I: Description and Numerical Tests, *J.*  
14 *Clim.*, 21(15), 3642–3659, 2008.
- 15 Myhre, G., Berntsen, T. K., Haywood, J. M., Sundet, J. K., Holben, B. N., Johnsrud, M. and Stordal, F.:  
16 Modeling the solar radiative impact of aerosols from biomass burning during the Southern African  
17 Regional Science Initiative (SAFARI-2000) experiment, *J. Geophys. Res. D: Atmos.*, 108(D13) [online]  
18 Available from: <https://onlinelibrary.wiley.com/doi/pdf/10.1029/2002JD002313>, 2003.
- 19 Myhre, G., Samset, B. H., Schulz, M., Balkanski, Y., Bauer, S., Berntsen, T. K., Bian, H., Bellouin, N.,  
20 Chin, M., Diehl, T., Easter, R. C., Feichter, J., Ghan, S. J., Hauglustaine, D., Iversen, T., Kinne, S.,  
21 Kirkevåg, A., Lamarque, J.-F., Lin, G., Liu, X., Lund, M. T., Luo, G., Ma, X., van Noije, T., Penner, J.  
22 E., Rasch, P. J., Ruiz, A., Seland, Ø., Skeie, R. B., Stier, P., Takemura, T., Tsigaridis, K., Wang, P.,  
23 Wang, Z., Xu, L., Yu, H., Yu, F., Yoon, J.-H., Zhang, K., Zhang, H. and Zhou, C.: Radiative forcing of  
24 the direct aerosol effect from AeroCom Phase II simulations, *Atmos. Chem. Phys.*, 13(4), 1853–1877,  
25 2013.
- 26 NASA Ames Earth Science Project Office: ORACLES Science Team: Suite of Aerosol, Cloud, and  
27 Related Data Acquired Aboard ER2 During ORACLES 2016, Version 1, ,  
28 doi:10.5067/Suborbital/ORACLES/ER2/2016\_V1, 2017a.
- 29 NASA Ames Earth Science Project Office: ORACLES Science Team: Suite of Aerosol, Cloud, and  
30 Related Data Acquired Aboard P3 During ORACLES 2016, Version 1, ,  
31 doi:10.5067/Suborbital/ORACLES/P3/2016\_V1, 2017b.
- 32 Neale, R. B., Chen, C.-C., Gettelman, A., Lauritzen, P. H., Park, S., Williamson, D. L., Conley, A. J.,  
33 Garcia, R., Kinnison, D., Lamarque, J.-F. and Others: Description of the NCAR community atmosphere  
34 model (CAM 5.0), *NCAR Tech. Note NCAR/TN-486+ STR*, 1(1), 1–12, 2010.
- 35 Park, R. J.: Sources of carbonaceous aerosols over the United States and implications for natural  
36 visibility, *J. Geophys. Res.*, 108(D12), 23,073, 2003.



- 1 Pauly, R. M., Yorks, J. E., Hlavka, D. L., McGill, M. J., Amiridis, V., Palm, S. P., Rodier, S. D.,  
2 Vaughan, M. A., Selmer, P. A., Kupchock, A. W., Baars, H. and Gialitaki, A.: Cloud Aerosol Transport  
3 System (CATS) 1064 nm Calibration and Validation, , doi:10.5194/amt-2019-172, 2019.
- 4 Peers, F., Waquet, F., Cornet, C., Dubuisson, P., Ducos, F., Goloub, P., Szczap, F., Tanré, D. and  
5 Thieuleux, F.: Absorption of aerosols above clouds from POLDER/PARASOL measurements and  
6 estimation of their direct radiative effect, *Atmos. Chem. Phys.*, 15(8), 4179–4196, 2015.
- 7 Petrenko, M., Kahn, R., Chin, M. and Limbacher, J.: Refined Use of Satellite Aerosol Optical Depth  
8 Snapshots to Constrain Biomass Burning Emissions in the GOCART Model: Refined BB Emission  
9 Correction for GOCART, *J. Geophys. Res. D: Atmos.*, 122(20), 10,983–11,004, 2017.
- 10 Petters, M. D. and Kreidenweis, S. M.: A single parameter representation of hygroscopic growth and  
11 cloud condensation nucleus activity, *Atmos. Chem. Phys.*, 7(8), 1961–1971, 2007.
- 12 Pistone, K., Redemann, J., Doherty, S., Zuidema, P., Burton, S., Cairns, B., Cochrane, S., Ferrare, R.,  
13 Flynn, C., Freitag, S., Howell, S., Kacenelenbogen, M., LeBlanc, S., Liu, X., Schmidt, K. S., Sedlacek, A.  
14 J., III, Segal-Rosenhaimer, M., Shinozuka, Y., Stammes, S., van Diedenhoven, B., Van Harten, G. and Xu,  
15 F.: Intercomparison of biomass burning aerosol optical properties from in-situ and remote-sensing  
16 instruments in ORACLES-2016, *Atmos. Chem. Phys. Discuss.*, 1–46, 2019.
- 17 Provencal, R., Gupta, M., Owano, T. G., Baer, D. S., Ricci, K. N., O’Keefe, A. and Podolske, J. R.:  
18 Cavity-enhanced quantum-cascade laser-based instrument for carbon monoxide measurements, *Appl.*  
19 *Opt.*, 44(31), 6712, 2005.
- 20 Rajapakshe, C., Zhang, Z., Yorks, J. E., Yu, H., Tan, Q., Meyer, K., Platnick, S. and Winker, D. M.:  
21 Seasonally transported aerosol layers over southeast Atlantic are closer to underlying clouds than  
22 previously reported: Smoke to Cloud Distance in SE Atlantic, *Geophys. Res. Lett.*, 44(11), 5818–5825,  
23 2017.
- 24 Randles, C. A., da Silva, A. M., Buchard, V., Colarco, P. R., Darmenov, A., Govindaraju, R., Smirnov,  
25 A., Holben, B., Ferrare, R., Hair, J., Shinozuka, Y. and Flynn, C. J.: The MERRA-2 Aerosol Reanalysis,  
26 1980 Onward. Part I: System Description and Data Assimilation Evaluation, *J. Clim.*, 30(17), 6823–6850,  
27 2017.
- 28 Rasch, P. J., Xie, S., Ma, P. -L, Lin, W., Wang, H., Tang, Q., Burrows, S. M., Caldwell, P., Zhang, K.,  
29 Easter, R. C., Cameron-Smith, P., Singh, B., Wan, H., Golaz, J. -C, Harrop, B. E., Roesler, E.,  
30 Bacmeister, J., Larson, V. E., Evans, K. J., Qian, Y., Taylor, M., Leung, L. R., Zhang, Y., Brent, L.,  
31 Branstetter, M., Hannay, C., Mahajan, S., Mامتjanov, A., Neale, R., Richter, J. H., Yoon, J. -H, Zender,  
32 C. S., Bader, D., Flanner, M., Foucar, J. G., Jacob, R., Keen, N., Klein, S. A., Liu, X., Salinger, A. G.,  
33 Shrivastava, M. and Yang, Y.: An Overview of the Atmospheric Component of the Energy Exascale  
34 Earth System Model, *J. Adv. Model. Earth Syst.*, doi:10.1029/2019MS001629, 2019.
- 35 Reddington, C. L., Carslaw, K. S., Stier, P., Schutgens, N., Coe, H., Liu, D., Allan, J., Browse, J., Pringle,  
36 K. J., Lee, L. A., Yoshioka, M., Johnson, J. S., Regayre, L. A., Spracklen, D. V., Mann, G. W., Clarke,



- 1 A., Hermann, M., Henning, S., Wex, H., Kristensen, T. B., Leaitch, W. R., Pöschl, U., Rose, D., Andreae,  
2 M. O., Schmale, J., Kondo, Y., Oshima, N., Schwarz, J. P., Nenes, A., Anderson, B., Roberts, G. C.,  
3 Snider, J. R., Leck, C., Quinn, P. K., Chi, X., Ding, A., Jimenez, J. L. and Zhang, Q.: The Global Aerosol  
4 Synthesis and Science Project (GASSP): Measurements and Modeling to Reduce Uncertainty, *Bull. Am.*  
5 *Meteorol. Soc.*, 98(9), 1857–1877, 2017.
- 6 Redemann, Wood, Zuidema, Doherty, Luna, LeBlanc, Diamond, Shinozuka, Ueyama, Pfister, DaSilva,  
7 Longo, Kacenelenbogen, Knox, Piketh, Haywood, Formenti, Mallet, Stier, Ackerman, Carmichael, Saide,  
8 Howell, Cairns, Knobelspiesse, Tanelli, L’Ecuyer, McFarquhar, Poellot, Nenes, Kacarab, Pui Shan  
9 Wong, Small-Griswold, Thornhill, Noone, Podolske, Schmidt, Sedlacek, Lang, Stith, Segal-Rozenhaimer,  
10 Hostetler, Ferrare, Burton, Diner, Platnick, Myers, Meyer, Spangenberg, Ian Chang: An overview of the  
11 ORACLES (ObseRvations of Aerosols above CLouds and their intERactionS) project: aerosol-cloud-  
12 radiation interactions in the Southeast Atlantic basin, in preparation.
- 13 Regayre, L. A., Johnson, J. S., Yoshioka, M., Pringle, K. J., Sexton, D. M. H., Booth, B. B. B., Lee, L. A.,  
14 Bellouin, N. and Carslaw, K. S.: Aerosol and physical atmosphere model parameters are both important  
15 sources of uncertainty in aerosol ERF, *Atmos. Chem. Phys.*, 18(13), 9975–10006, 2018.
- 16 Rienecker, M. M., Suarez, M. J., Todling, R., Bacmeister, J., Takacs, L., -C. Liu, H., Gu, W.,  
17 Sienkiewicz, M., Koster, R. D., Gelaro, R., Stajner, I. and Nielsen, J. E.: The GEOS-5 Data Assimilation  
18 System— Documentation of Versions 5.0.1, 5.1.0, and 5.2.0, [online] Available from:  
19 <https://gmao.gsfc.nasa.gov/pubs/docs/Rienecker369.pdf>, 2008.
- 20 Rogers, R. R., Hair, J. W., Hostetler, C. A., Ferrare, R. A., Obland, M. D., Cook, A. L., Harper, D. B.,  
21 Burton, S. P., Shinozuka, Y., McNaughton, C. S., Clarke, A. D., Redemann, J., Russell, P. B., Livingston,  
22 J. M. and Kleinman, L. I.: NASA LaRC airborne high spectral resolution lidar aerosol measurements  
23 during MILAGRO: observations and validation, *Atmos. Chem. Phys.*, 9(14), 4811–4826, 2009.
- 24 Saide, P. E., Thompson, G., Eidhammer, T., da Silva, A. M., Bradley Pierce, R. and Carmichael, G. R.:  
25 Assessment of biomass burning smoke influence on environmental conditions for multiyear tornado  
26 outbreaks by combining aerosol-aware microphysics and fire emission constraints, *Journal of*  
27 *Geophysical Research: Atmospheres*, 121(17), 10,294–10,311, doi:10.1002/2016jd025056, 2016.
- 28 Sakaeda, N., Wood, R. and Rasch, P. J.: Direct and semidirect aerosol effects of southern African  
29 biomass burning aerosol, *J. Geophys. Res.*, 116(D12), doi:10.1029/2010jd015540, 2011.
- 30 Schwarz, J. P., Gao, R. S., Fahey, D. W., Thomson, D. S., Watts, L. A., Wilson, J. C., Reeves, J. M.,  
31 Darbeheshti, M., Baumgardner, D. G., Kok, G. L., Chung, S. H., Schulz, M., Hendricks, J., Lauer, A.,  
32 Kärcher, B., Slowik, J. G., Rosenlof, K. H., Thompson, T. L., Langford, A. O., Loewenstein, M. and  
33 Aikin, K. C.: Single-particle measurements of midlatitude black carbon and light-scattering aerosols from  
34 the boundary layer to the lower stratosphere, *J. Geophys. Res.*, 111(D16), D16207,  
35 doi:10.1029/2006JD007076, 2006.
- 36 Schwarz, J. P., Spackman, J. R., Gao, R. S., Perring, A. E., Cross, E., Onasch, T. B., Ahern, A., Wrobel,  
37 W., Davidovits, P., Olfert, J., Dubey, M. K., Mazzoleni, C. and Fahey, D. W.: The Detection Efficiency



- 1 of the Single Particle Soot Photometer, *Aerosol Sci. Technol.*, 44(8), 612–628, 2010.
- 2 Shank, L. M., Howell, S., Clarke, A. D., Freitag, S., Brekhovskikh, V., Kapustin, V., McNaughton, C.,  
3 Campos, T. and Wood, R.: Organic matter and non-refractory aerosol over the remote Southeast Pacific:  
4 oceanic and combustion sources, *Atmos. Chem. Phys.*, 12(1), 557–576, 2012.
- 5 Shipley, S. T., Tracy, D. H., Eloranta, E. W., Trauger, J. T., Sroga, J. T., Roesler, F. L. and Weinman, J.  
6 A.: High spectral resolution lidar to measure optical scattering properties of atmospheric aerosols. 1:  
7 Theory and instrumentation, *Appl. Opt.*, AO, 22(23), 3716–3724, 1983.
- 8 Song, X. and Zhang, G. J.: Microphysics parameterization for convective clouds in a global climate  
9 model: Description and single-column model tests, *J. Geophys. Res.*, 116(D2), 6837, 2011.
- 10 Stephens, M., Turner, N. and Sandberg, J.: Particle Identification by Laser-Induced Incandescence in a  
11 Solid-State Laser Cavity, *Appl. Opt.*, 42(19), 3726–3736, 2003.
- 12 Stier, P., Schutgens, N. A. J., Bellouin, N., Bian, H., Boucher, O., Chin, M., Ghan, S., Huneeus, N.,  
13 Kinne, S., Lin, G., Ma, X., Myhre, G., Penner, J. E., Randles, C. A., Samset, B., Schulz, M., Takemura,  
14 T., Yu, F., Yu, H. and Zhou, C.: Host model uncertainties in aerosol radiative forcing estimates: results  
15 from the AeroCom Prescribed intercomparison study, *Atmos. Chem. Phys.*, 13(6), 3245–3270, 2013.
- 16 Sueper, D.: ToF-AMS Software Downloads, online available at:  
17 <http://cires.colorado.edu/jimenezgroup/ToFAMSResources/ToFSoftware/index.html>, accessed February  
18 2018, 2018.
- 19 Swap, R. J., Annegarn, H. J., Suttles, J. T., King, M. D., Platnick, S., Privette, J. L. and Scholes, R. J.:  
20 Africa burning: A thematic analysis of the Southern African Regional Science Initiative (SAFARI 2000),  
21 *J. Geophys. Res. D: Atmos.*, 108(D13), doi:10.1029/2003jd003747, 2003.
- 22 Textor, C., Schulz, M., Guibert, S., Kinne, S., Balkanski, Y., Bauer, S., Berntsen, T., Berglen, T.,  
23 Boucher, O., Chin, M. and Others: Analysis and quantification of the diversities of aerosol life cycles  
24 within AeroCom, *Atmos. Chem. Phys.*, 6(7), 1777–1813, 2006.
- 25 Virkkula, A.: Correction of the Calibration of the 3-wavelength Particle Soot Absorption Photometer (3λ  
26 PSAP), *Aerosol Sci. Technol.*, 44(8), 706–712, 2010.
- 27 Voldoire, A., Decharme, B., Pianezze, J., Lebeaupin Brossier, C., Sevault, F., Seyfried, L., Garnier, V.,  
28 Bielli, S., Valcke, S., Alias, A., Accensi, M., Arduin, F., Bouin, M.-N., Ducrocq, V., Faroux, S.,  
29 Giordani, H., Léger, F., Marsaleix, P., Rainaud, R., Redelsperger, J.-L., Richard, E. and Riette, S.:  
30 SURFEX v8.0 interface with OASIS3-MCT to couple atmosphere with hydrology, ocean, waves and sea-  
31 ice models, from coastal to global scales, *Geoscientific Model Development*, 10(11), 4207–4227, 2017.
- 32 Wang, J.: Geostationary satellite retrievals of aerosol optical thickness during ACE-Asia, *J. Geophys.*  
33 *Res.*, 108(D23), 17,969, 2003a.
- 34 Wang, J.: GOES 8 retrieval of dust aerosol optical thickness over the Atlantic Ocean during PRIDE, J.



- 1 Geophys. Res., 108(D19), 57, 2003b.
- 2 Wang, Q., Jacob, D. J., Fisher, J. A., Mao, J., Leibensperger, E. M., Carouge, C. C., Sager, P. L., Kondo,  
3 Y., Jimenez, J. L., Cubison, M. J. and Doherty, S. J.: Sources of carbonaceous aerosols and deposited  
4 black carbon in the Arctic in winter-spring: implications for radiative forcing, *Atmos. Chem. Phys.*,  
5 11(23), 12453–12473, 2011.
- 6 Wang, Q., Jacob, D. J., Spackman, J. R., Perring, A. E., Schwarz, J. P., Moteki, N., Marais, E. A., Ge, C.,  
7 Wang, J. and Barrett, S. R. H.: Global budget and radiative forcing of black carbon aerosol: Constraints  
8 from pole-to-pole (HIPPO) observations across the Pacific, *J. Geophys. Res. D: Atmos.*, 119(1), 195–206,  
9 2014.
- 10 Waquet, F., Peers, F., Ducos, F., Goloub, P., Platnick, S., Riedi, J., Tanré, D. and Thieuleux, F.: Global  
11 analysis of aerosol properties above clouds, *Geophys. Res. Lett.*, 40(21), 5809–5814, 2013.
- 12 Wesely, M. L.: Parameterization of surface resistances to gaseous dry deposition in regional-scale  
13 numerical models, *Atmospheric Environment (1967)*, 23(6), 1293–1304, doi:10.1016/0004-  
14 6981(89)90153-4, 1989.
- 15 Wilson, D. R. and Ballard, S. P.: A microphysically based precipitation scheme for the UK  
16 meteorological office unified model, *Q.J. Royal Met. Soc.*, 125(557), 1607–1636, 1999.
- 17 Wilson, D. R., Bushell, A. C., Kerr-Munslow, A. M., Price, J. D. and Morcrette, C. J.: PC2: A prognostic  
18 cloud fraction and condensation scheme. I: Scheme description, *Q.J.R. Meteorol. Soc.*, 134(637), 2093–  
19 2107, 2008.
- 20 Wood, R., Mechoso, C. R., Bretherton, C. S., Weller, R. A., Huebert, B., Straneo, F., Albrecht, B. A.,  
21 Coe, H., Allen, G., Vaughan, G. and Others: The VAMOS ocean-cloud-atmosphere-land study regional  
22 experiment (VOCALS-REx): goals, platforms, and field operations, *Atmos. Chem. Phys.*, 11(2), 627–  
23 654, 2011.
- 24 Wyant, M. C., Wood, R., Bretherton, C. S., Mechoso, C. R., Bacmeister, J., Balmaseda, M. A., Barrett,  
25 B., Codron, F., Earnshaw, P., Fast, J., Hannay, C., Kaiser, J. W., Kitagawa, H., Klein, S. A., Köhler, M.,  
26 Manganello, J., Pan, H.-L., Sun, F., Wang, S. and Wang, Y.: The PreVOCA experiment: modeling the  
27 lower troposphere in the Southeast Pacific, *Atmos. Chem. Phys.*, 10(10), 4757–4774, 2010.
- 28 Wyant, M. C., Bretherton, C. S., Wood, R., Carmichael, G. R., Clarke, A., Fast, J., George, R., Gustafson,  
29 W. I., Jr., Hannay, C., Lauer, A., Lin, Y., Morcrette, J.-J., Mulcahy, J., Saide, P. E., Spak, S. N. and Yang,  
30 Q.: Global and regional modeling of clouds and aerosols in the marine boundary layer during VOCALS:  
31 the VOCA intercomparison, *Atmos. Chem. Phys.*, 15(1), 153–172, 2015.
- 32 Xie, S., Lin, W., Rasch, P. J., Ma, P.-L., Neale, R., Larson, V. E., Qian, Y., Bogenschütz, P. A., Caldwell,  
33 P., Cameron-Smith, P., Golaz, J.-C., Mahajan, S., Singh, B., Tang, Q., Wang, H., Yoon, J.-H., Zhang, K.  
34 and Zhang, Y.: Understanding Cloud and Convective Characteristics in Version 1 of the E3SM  
35 Atmosphere Model, *Journal of Advances in Modeling Earth Systems*, 10(10), 2618–2644,



- 1 doi:10.1029/2018ms001350, 2018.
- 2 Zaveri, R. A. and Peters, L. K.: A new lumped structure photochemical mechanism for large-scale  
3 applications, *J. Geophys. Res.*, 104(D23), 30387–30415, 1999.
- 4 Zhang, G. J. and McFarlane, N. A.: Sensitivity of climate simulations to the parameterization of cumulus  
5 convection in the Canadian climate centre general circulation model, *Atmosphere-Ocean*, 33(3), 407–446,  
6 1995.
- 7 Zhang, L., Gong, S., Padro, J. and Barrie, L.: A size-segregated particle dry deposition scheme for an  
8 atmospheric aerosol module, *Atmos. Environ.*, 35(3), 549–560, 2001.
- 9 Zhang, Y., Zhang, X., Wang, K., He, J., Leung, L. R., Fan, J. and Nenes, A.: Incorporating an advanced  
10 aerosol activation parameterization into WRF-CAM5: Model evaluation and parameterization  
11 intercomparison: An Advanced Aerosol Activation Scheme, *J. Geophys. Res. D: Atmos.*, 120(14), 6952–  
12 6979, 2015.
- 13 Zhu, C., Kobayashi, H., Kanaya, Y. and Saito, M.: Size-dependent validation of MODIS MCD64A1  
14 burned area over six vegetation types in boreal Eurasia: Large underestimation in croplands, *Sci. Rep.*,  
15 7(1), 4181, 2017.
- 16 Zuidema, P., Redemann, J., Haywood, J., Wood, R., Piketh, S., Hipondoka, M. and Formenti, P.: Smoke  
17 and clouds above the southeast Atlantic: Upcoming field campaigns probe absorbing aerosol's impact on  
18 climate, *Bull. Am. Meteorol. Soc.*, 97(7), 1131–1135, 2016.



1 **Table 1. Specifications of the observations used in this study.**

Instrument [platform]	Primary measurement	Temporal resolution
SP2 [P3]	Black carbon mass per particle, 90–500 nm	Particle by particle
Time of Flight (ToF) – Aerodyne aerosol mass spectrometer (AMS) [P3]	Non-refractory aerosol composition (~ 50 to 500 nm vacuum aerodynamic diameter)	5s
UHSAS, ultra-high sensitivity aerosol spectrometer [P3]	Number size distribution for dry particle diameters between 60 and 1000 nm	1s
Nephelometer [P3]	Submicron dry particle scattering coefficient at 450, 550, 700 nm	6s
PSAP, particle soot absorption photometer [P3]	Submicron dry particle light absorption at 470, 530 and 660 nm	1-60s depending on concentration
4STAR, an airborne sun-/sky-photometer [P3]	Hyperspectral direct solar beam transmittance, AOD; values at 550 nm	1s
HSRL-2, the NASA Langley 2nd generation airborne High Spectral Resolution Lidar [ER2]	Aerosol backscattering and extinction coefficients, values at 532 nm	10s for aerosol backscatter coefficient and 60s for aerosol extinction coefficient
CO/CO <sub>2</sub> /H <sub>2</sub> O Analyzer [P3]	Carbon monoxide	1s



1 **Table 2. Model specifications.**

Model	Domain extent	Horizontal grid spacing	Vertical levels (> and < 700 hPa)	initializing meteorology	Initializati on frequency	Aerosol scheme	PMBL scheme	Fire emissions source	Emission temporal resolution
WRF-CAM5	41S-14N, 34W-51E	36 km	75, 50	NCEP Final Analysis	5 days	MAM3	Bretherton and Park (2009)	QFED2	Daily
GEOS-5	Global	25 by 31 km	72, 17	MERRA-2	Daily	AeroChem (GOCART)	TURBDAY	QFED2	Daily
GEOS-Chem	Global	2.5° by 2 (lon, lat)	17, 55	GEOS-FP	Hourly	GEOS-Chem standard	VDIFF: non-local scheme formulated by Holtzlag and Boville (1993)	QFED2	Daily
EAM-E3SM	Global	100 km	72, 17	ERA-INT	Every 3 hours	MAM4	CLUBB (Larson and Golaz, 2005)	GFED*	Monthly
Unified Model	Global	61 by 92 km	65, 20	ERA-INT	Every 6 hours	GLOMAP-mode	Lock et al. (2000)	FEER	Daily
ALADIN-Climate	37S-9N; 33W-45E	12 km	34, 6	ERA-INT	Once	Interactive		GFED	Monthly

\*IPCC AR5 emissions, based on GFED emissions averaged between 1997-2002.

2  
 3  
 4  
 5



1 **Table 3. Comparison of flight-day values to the monthly-mean climatology formulated from**  
 2 **the same model. Shown are the mean bias (MB), and root-mean-square deviation (RMSD),**  
 3 **as well as their ratio (%) to the monthly mean.**

	WRF-CAM5		GEOS-5	
	MB	RMSD	MB	RMSD
<i>Smoke Top Height (m) simulated as observed by HSRL-2 on ER2</i>				
	+125 (+3%)	500 (11%)	+369 (+11%)	505 (15%)
<i>Smoke Base Height (m) simulated as observed by HSRL-2 on ER2</i>				
	+371 (+29%)	426 (33%)	+103 (+8%)	292 (23%)
<i>Black Carbon Mass (ng m<sup>-3</sup>)</i>				
3-6 km	-4.5 (-1%)	182.5 (27%)	-1.8 (-0%)	198.2 (30%)
FT≤ 3km	+161.1 (+25%)	319.3 (50%)	-98.8 (-9%)	423.6 (38%)
MBL	+40.1 (+31%)	80.3 (63%)	+82.1 (+21%)	354.2 (93%)
<i>Organic Aerosol Mass (ug m<sup>-3</sup>)</i>				
3-6 km	-0.0 (-0%)	1.5 (27%)	+0.0 (+0%)	2.9 (32%)
FT≤ 3km	+1.3 (+25%)	2.6 (50%)	-1.6 (-10%)	6.2 (40%)



MBL	+0.3 (+36%)	0.6 (70%)	+1.0 (+19%)	4.9 (92%)
-----	----------------	--------------	----------------	--------------

*Sulfate Aerosol Mass ( $\mu\text{g m}^{-3}$ )*

3-6 km	-0.1 (-4%)	0.2 (19%)	--	--
-----------	---------------	--------------	----	----

FT $\leq$ 3km	+0.2 (+17%)	0.4 (31%)	--	--
------------------	----------------	--------------	----	----

MBL	+0.1 (+13%)	0.3 (44%)	--	--
-----	----------------	--------------	----	----

*Volumetric Mean Diameter (nm)*

3-6 km	-7 (-3%)	10 (4%)	--	--
-----------	-------------	------------	----	----

FT $\leq$ 3km	-6 (-2%)	17 (6%)	--	--
------------------	-------------	------------	----	----

MBL	-22 (-7%)	37 (12%)	--	--
-----	--------------	-------------	----	----

*Aerosol Optical Depth simulated as observed by HSRL-2 on ER2*

Above clouds	+0.018 (+7%)	0.055 (21%)	+0.001 (+1%)	0.036 (16%)
-----------------	-----------------	----------------	-----------------	----------------

*Aerosol Optical Depth simulated as observed by 4STAR on P3*

Above clouds	+0.031 (+12%)	0.048 (18%)	-0.019 (-9%)	0.057 (26%)
-----------------	------------------	----------------	-----------------	----------------

*Extinction Coefficient ( $\text{Mm}^{-1}$ ) simulated as observed by HSRL-2 on ER2*



3-6 km	+3 (+7%)	12 (23%)	+2 (+5%)	12 (30%)
--------	-------------	-------------	-------------	-------------

*Extinction Coefficient ( $Mm^{-1}$ ) simulated as observed by  
 neph+PSAP on P3*

3-6 km	-1 (-3%)	13 (25%)	-1 (-3%)	14 (33%)
--------	-------------	-------------	-------------	-------------

FT $\leq$ 3km	+11 (+22%)	22 (42%)	-8 (-13%)	24 (39%)
------------------	---------------	-------------	--------------	-------------

MBL	-2 (-6%)	10 (32%)	+7 (+6%)	67 (62%)
-----	-------------	-------------	-------------	-------------

*Scattering Ångström Exponent*

3-6 km	+0.1 (+5%)	0.1 (6%)	+0.0 (+0%)	0.0 (2%)
--------	---------------	-------------	---------------	-------------

FT $\leq$ 3k m	+0.0 (+4%)	0.1 (12%)	+0.0 (+2%)	0.1 (6%)
-------------------	---------------	--------------	---------------	-------------

MBL	+0.1 (+29%)	0.2 (44%)	+0.1 (+10%)	0.2 (30%)
-----	----------------	--------------	----------------	--------------

*Absorption Ångström Exponent*

3-6 km	+0.0 (+1%)	0.0 (1%)	+0.0 (+0%)	0.0 (0%)
--------	---------------	-------------	---------------	-------------

FT $\leq$ 3k m	+0.0 (+0%)	0.0 (2%)	-0.0 (-0%)	0.0 (1%)
-------------------	---------------	-------------	---------------	-------------

MBL	+0.0 (+1%)	0.1 (5%)	-0.0 (-0%)	0.0 (2%)
-----	---------------	-------------	---------------	-------------

*Single Scattering Albedo*

3-6 km	-0.00 (-0%)	0.01 (1%)	-0.00 (-0%)	0.01 (1%)
--------	----------------	--------------	----------------	--------------



FT≤3k	-0.01	0.01	-0.00	0.01
m	(-1%)	(2%)	(-0%)	(1%)

MBL	-0.02	0.03	-0.01	0.01
	(-2%)	(3%)	(-1%)	(1%)

*Carbon Monoxide (ppbv)*

3-6	+0	23	+0	22
km	(+0%)	(15%)	(+0%)	(13%)

FT≤	+12	29	-2	26
3km	(+10%)	(23%)	(-2%)	(16%)

MBL	+3	5	+1	12
	(+5%)	(7%)	(+2%)	(15%)

- 1
- 2 The optical properties are at 500-550 nm. The values are for the P3 flights unless otherwise
- 3 noted, in the diagonally and horizontally aligned boxes.



1 **Table 4. The differences of box-average model values from the observations. Shown are the**  
 2 **mean bias (MB), and root-mean-square deviation (RMSD), as well as their ratio (%) to the**  
 3 **observed mean.**

4

	WRF-CAM5		GEOS-5		GEOS-Chem		EAM-E3SM		UM		ALADIN-Climate	
	MB	RMSD	MB	RMSD	MB	RMSD	MB	RMSD	MB	RMSD	MB	RMSD
<i>Smoke Top Height (m) compared to HSRL-2 on ER2</i>												
	-167	415	-456	596	-473	763	-114	460	+6	440	-176	830
	(-3%)	(9%)	(-9%)	(12%)	(-10%)	(16%)	(-2%)	(10%)	(+0%)	(9%)	(-4%)	(17%)
<i>Smoke Base Height (m) compared to HSRL-2 on ER2</i>												
	-422	553	-1401	1424	-877	938	-688	784	-616	709	-299	566
	(-21%)	(27%)	(-69%)	(70%)	(-43%)	(46%)	(-34%)	(38%)	(-31%)	(35%)	(-15%)	(28%)
<i>Black Carbon Mass (ng m<sup>-3</sup>)</i>												
3-6 km	+60.4	171.4	+47.4	206.1	+7.9	283.0	-256.6	287.1	-234.6	279.0	--	--
	(+10%)	(28%)	(+8%)	(34%)	(+1%)	(47%)	(-42%)	(47%)	(-39%)	(46%)	--	--
FT ≤3km	-13.0	456.1	+162.1	527.5	-1.6	392.3	-524.8	655.9	-140.2	312.9	--	--
	(-2%)	(56%)	(+19%)	(62%)	(-0%)	(46%)	(-61%)	(77%)	(-16%)	(37%)	--	--
MBL	-8.2	118.2	+288.3	552.8	+79.4	236.8	+2.7	97.7	-48.6	93.9	--	--
	(-5%)	(67%)	(+163%)	(313%)	(+45%)	(134%)	(+1%)	(52%)	(-28%)	(53%)	--	--
<i>Organic Aerosol Mass (ug m<sup>-3</sup>)</i>												
3-6 km	+0.0	2.3	+3.5	5.0	+1.8	4.0	+5.3	5.7	-1.9	2.9	--	--
	(+0%)	(42%)	(+63%)	(89%)	(+32%)	(71%)	(+95%)	(103%)	(-34%)	(52%)	--	--
FT ≤3km	+0.7	3.0	+7.7	9.2	+3.6	5.4	+2.8	4.1	+0.5	3.1	--	--
	(+12%)	(53%)	(+117%)	(140%)	(+55%)	(82%)	(+43%)	(62%)	(+8%)	(47%)	--	--
MBL	+0.3	0.8	+5.4	8.9	+2.1	3.9	+3.7	5.1	+0.3	0.9	--	--
	(+26%)	(83%)	(+546%)	(901%)	(+210%)	(392%)	(+352%)	(494%)	(+27%)	(96%)	--	--
<i>Sulfate Aerosol Mass (ug m<sup>-3</sup>)</i>												
3-6 km	+0.5	0.6	--	--	--	--	+0.2	0.3	-0.4	0.6	--	--
	(+67%)	(79%)	--	--	--	--	(+21%)	(43%)	(-56%)	(74%)	--	--
FT ≤3km	+0.4	0.7	--	--	--	--	+0.1	0.5	-0.7	1.0	--	--
	(+37%)	(55%)	--	--	--	--	(+4%)	(42%)	(-56%)	(75%)	--	--



MBL	-0.5 (-38%)	0.7 (60%)	--	--	--	--	+1.2 (+94%)	1.5 (121%)	-0.5 (-45%)	0.8 (67%)	--	--																										
<i>Volumetric Mean Diameter (nm)</i>																																						
3-6 km	+42 (+21%)	43 (21%)	--	--	--	--	--	--	+64/+12 1 (+32/+6 0%)	65/121 (32/60%)	--	--																										
FT ≤3km	+81 (+42%)	83 (43%)	--	--	--	--	--	--	+72/+11 6 (+37/+6 0%)	73/117 (37/60%)	--	--																										
MBL	+98 (+48%)	105 (52%)	--	--	--	--	--	--	+40/+21 5 (+20/+10 6%)	46/217 (23/107%)	--	--																										
<table border="0" style="width: 100%; border-collapse: collapse;"> <thead> <tr> <th style="width: 15%;"></th> <th colspan="2" style="text-align: center;">WRF-CAM5</th> <th colspan="2" style="text-align: center;">GEOS-5</th> <th colspan="2" style="text-align: center;">GEOS-Chem</th> <th colspan="2" style="text-align: center;">EAM-E3SM</th> <th colspan="2" style="text-align: center;">UM</th> <th colspan="2" style="text-align: center;">ALADIN-Climate</th> </tr> <tr> <th></th> <th style="text-align: center;">MB</th> <th style="text-align: center;">RMSD</th> </tr> </thead> </table>														WRF-CAM5		GEOS-5		GEOS-Chem		EAM-E3SM		UM		ALADIN-Climate			MB	RMSD										
	WRF-CAM5		GEOS-5		GEOS-Chem		EAM-E3SM		UM		ALADIN-Climate																											
	MB	RMSD	MB	RMSD	MB	RMSD	MB	RMSD	MB	RMSD	MB	RMSD																										
<i>Aerosol Optical Depth compared to HSRL-2 on ER2</i>																																						
Above clouds	-0.042 (-12%)	0.077 (23%)	-0.101 (-30%)	0.123 (37%)	+0.138 (+42%)	0.189 (57%)	+0.069 (+21%)	0.093 (28%)	0.053 (-16%)	0.087 (26%)	-0.108 (-32%)	0.125 (37%)																										
<i>Aerosol Optical Depth compared to 4STAR on P3</i>																																						
Above clouds	-0.068 (-19%)	0.098 (28%)	-0.134 (-40%)	0.183 (55%)	+0.008 (+3%)	0.103 (31%)	+0.055 (+16%)	0.088 (26%)	-0.155 (-46%)	0.184 (55%)	-0.106 (-32%)	0.140 (42%)																										
<i>Extinction Coefficient (Mm<sup>-1</sup>) compared to HSRL-2 on ER2</i>																																						
3-6 km	-16 (-23%)	23 (32%)	-28 (-38%)	32 (44%)	+24 (+33%)	33 (45%)	+1 (+1%)	17 (23%)	-43/-19 (-59/- 26%)	49/23 (66/31%)	--	--																										
<i>Extinction Coefficient (Mm<sup>-1</sup>) compared to neph+PSAP on P3</i>																																						
3-6 km	-25 (-34%)	29 (39%)	-34 (-46%)	36 (49%)	+5 (+6%)	41 (56%)	-8 (-11%)	20 (27%)	-57/-48 (-77/- 65%)	58/49 (78/66%)	--	--																										
FT ≤3km	-8 (-11%)	34 (48%)	-22 (-29%)	39 (51%)	+14 (+18%)	33 (43%)	+6 (+8%)	21 (27%)	-40/-26 (-53/- 35%)	49/35 (65/47%)	--	--																										



MBL	-13 (-32%)	23 (54%)	+73 (+175%)	119 (285%)	+54 (+128%)	75 (181%)	+104 (+269%)	115 (297%)	-18/+55 (-44/+132%)	27/64 (64/153%)	--	--
<i>Scattering Ångström Exponent</i>												
3-6 km	-0.6 (-35%)	0.6 (36%)	-0.1 (-4%)	0.1 (6%)	+0.0 (+0%)	0.1 (3%)	--	--	+0.0/-0.0 (+2/-2%)	0.1/0.1 (3/8%)	--	--
FT ≤3km	-0.8 (-45%)	0.8 (46%)	-0.0 (-1%)	0.1 (7%)	+0.1 (+3%)	0.1 (5%)	--	--	+0.0/-0.0 (+2/-1%)	0.1/0.1 (6/6%)	--	--
MBL	-0.7 (-53%)	0.8 (57%)	-0.7 (-52%)	0.8 (59%)	-0.5 (-34%)	0.7 (48%)	--	--	-0.4/-0.6 (-27/-40%)	0.6/0.7 (45/50%)	--	--
<i>Absorption Ångström Exponent</i>												
3-6 km	-0.4 (-27%)	0.4 (27%)	-0.4 (-27%)	0.4 (28%)	-0.4 (-25%)	0.4 (25%)	--	--	-0.1/-0.2 (-5/-10%)	0.1/0.2 (7/12%)	--	--
FT ≤3km	-0.5 (-30%)	0.5 (30%)	-0.4 (-27%)	0.4 (27%)	-0.4 (-23%)	0.4 (24%)	--	--	-0.1/-0.2 (-8/-10%)	0.1/0.2 (9/11%)	--	--
MBL	-0.3 (-23%)	0.6 (41%)	-0.2 (-16%)	0.6 (43%)	-0.3 (-22%)	0.7 (44%)	--	--	+0.0/-0.3 (+3/-20%)	0.5/0.8 (33/54%)	--	--
<i>Single Scattering Albedo</i>												
3-6 km	-0.03 (-3%)	0.03 (4%)	-0.01 (-2%)	0.02 (2%)	+0.07 (+8%)	0.07 (8%)	+0.02 (+3%)	0.03 (3%)	-0.07/-0.01 (-8/-2%)	0.07/0.02 (8/3%)	--	--
FT ≤3km	+0.01 (+1%)	0.02 (2%)	-0.00 (-0%)	0.01 (2%)	+0.08 (+10%)	0.08 (10%)	+0.08 (+9%)	0.08 (9%)	0.03/+0.01 (-4/+1%)	0.04/0.02 (4/3%)	--	--
MBL	+0.03 (+4%)	0.07 (8%)	+0.08 (+9%)	0.10 (11%)	+0.10 (+11%)	0.11 (12%)	+0.08 (+8%)	0.09 (10%)	+0.07/+0.10 (+8/+12%)	0.09/0.11 (11/13%)	--	--



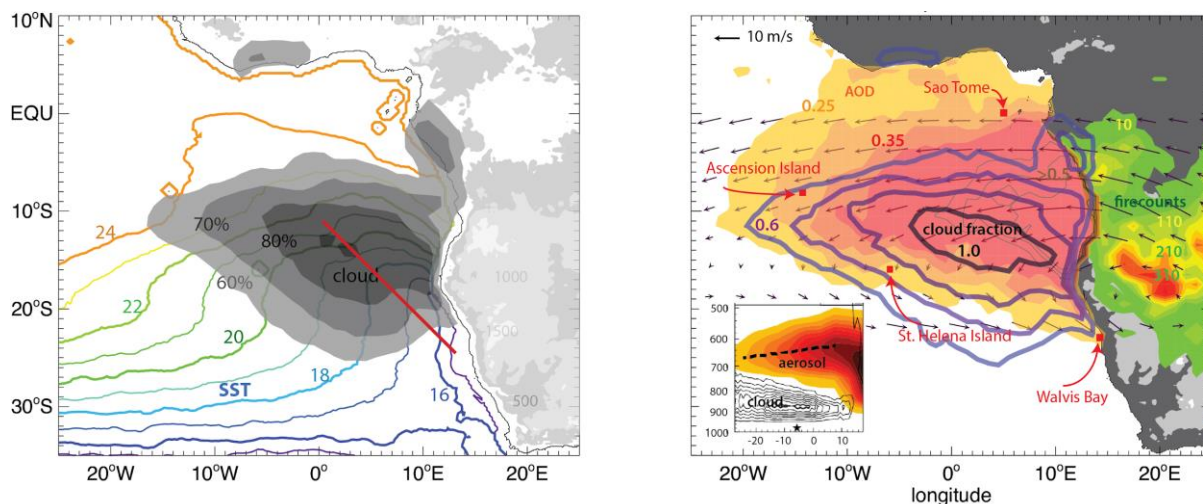
Carbon Monoxide (ppbv)

3-6 km	-37 (-20%)	44 (23%)	-19 (-10%)	30 (16%)	-38 (-20%)	45 (24%)	--	--	--	--	--	--
FT ≤3km	-25 (-15%)	44 (27%)	-14 (-8%)	33 (19%)	-9 (-5%)	36 (21%)	--	--	--	--	--	--
MBL	-20 (-22%)	24 (26%)	-10 (-11%)	21 (22%)	-4 (-4%)	19 (20%)	--	--	--	--	--	--

1  
 2 The optical properties are at 500-550 nm. The values are for the P3 flights unless otherwise  
 3 noted, in the diagonally and horizontally aligned boxes. The hyphens indicate products  
 4 unavailable. For UM the pair of values, where given, correspond to dry and ambient humidity  
 5 conditions in this order.



1

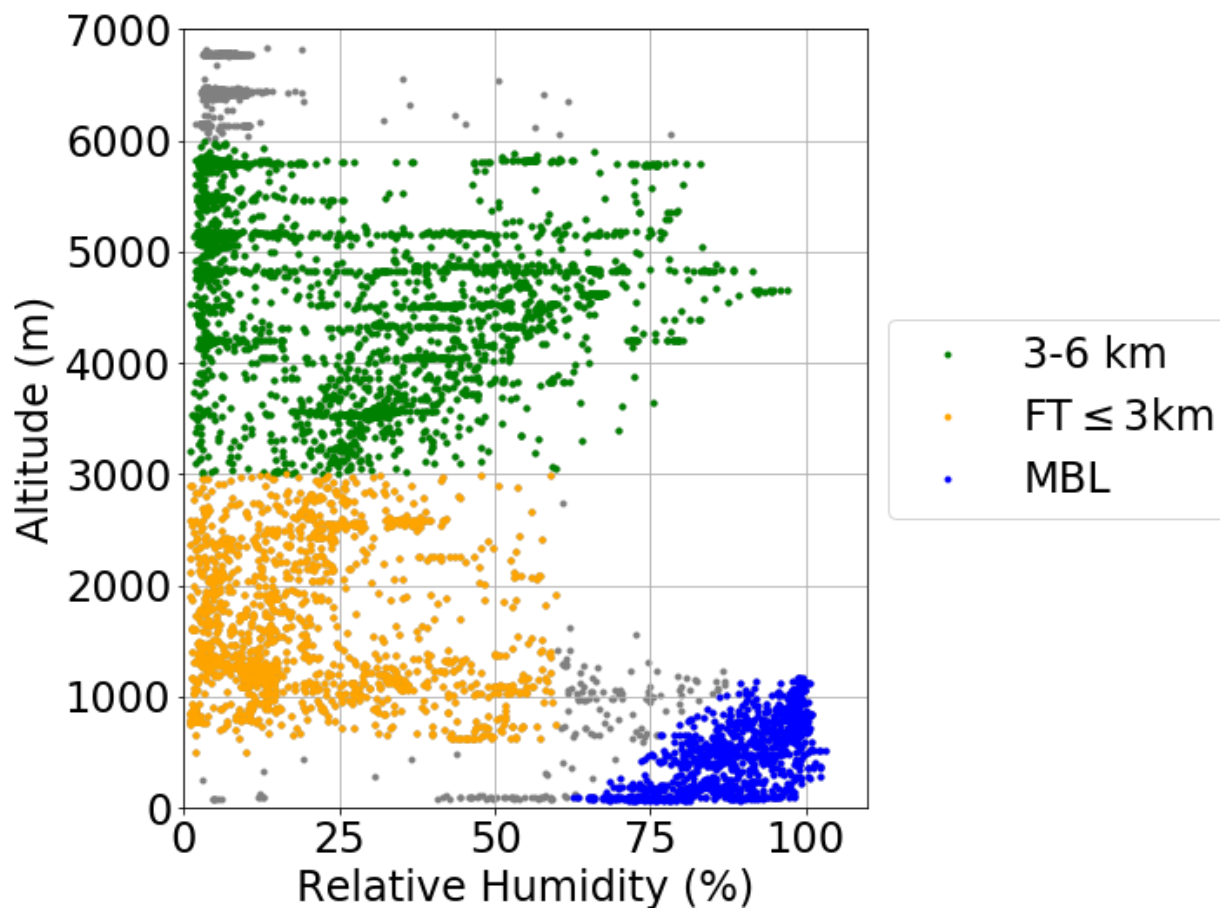


2

3 **Fig. 1. (a) September 2003-2016 WindSat sea surface temperature climatology (colored**  
4 **contours) and 2000-2016 Terra MODIS low cloud fraction climatology (gray shaded**  
5 **contours), with the routine flight track superimposed (red line). (b) September-mean**  
6 **climatology of MODIS low-level cloud fraction (2002-2012; blue to black contours, 0.6-1.0**  
7 **increments of 0.1), fine-mode aerosol optical depth (yellow-red shading indicates 0.25-0.45**  
8 **in increments of 0.05 and very light black contour lines indicate 0.5-0.7 in increments of**  
9 **0.1), and fire pixel counts (green-red shading, 50-310 fire counts per 1° box in increments**  
10 **of 50), and ERA-Interim 2002-2012 600-hPa winds (referenced at 10 m/s). Inset:**  
11 **September-mean a 6°S-17°S latitude cross-section of CALIOP smoke aerosol count (2006-**  
12 **2012) and CloudSat cloud fraction (2006-2010). The CloudSat cloud fraction are calculated**  
13 **following Stein et al. (2011). Right panel figure reproduced from Zuidema et al. (2016). ©**  
14 **American Meteorological Society. Used with permission.**



1

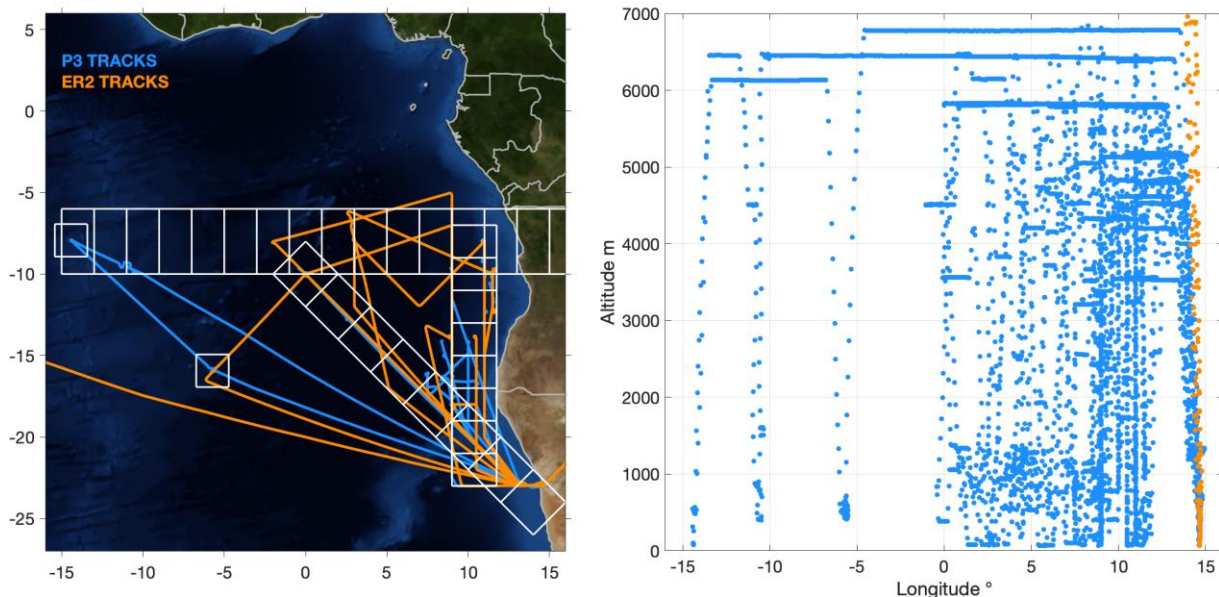


2

3 **Fig. 2.** Observed vertical profiles of relative humidity, derived from the dew point  
4 measurements. The blue, orange and green markers indicate MBL, the lower FT and mid  
5 FT, respectively, as defined in text. The grey markers indicate the data that do not belong to  
6 either group, most of them in the inversion.



1



2

3 **Fig. 3:** (left) The boxes selected for the model-observation comparison, overlaid on the P3  
4 and ER2 flight paths (with HSRL-2 observations) from September 2016 and NASA's Blue  
5 Marble: Next Generation surface image, courtesy of NASA's Earth Observatory. (right) The  
6 altitude and longitude of the flights averaged over 60s. The ER2 was at altitude of about 20  
7 km except for take-off and landing.

8

9

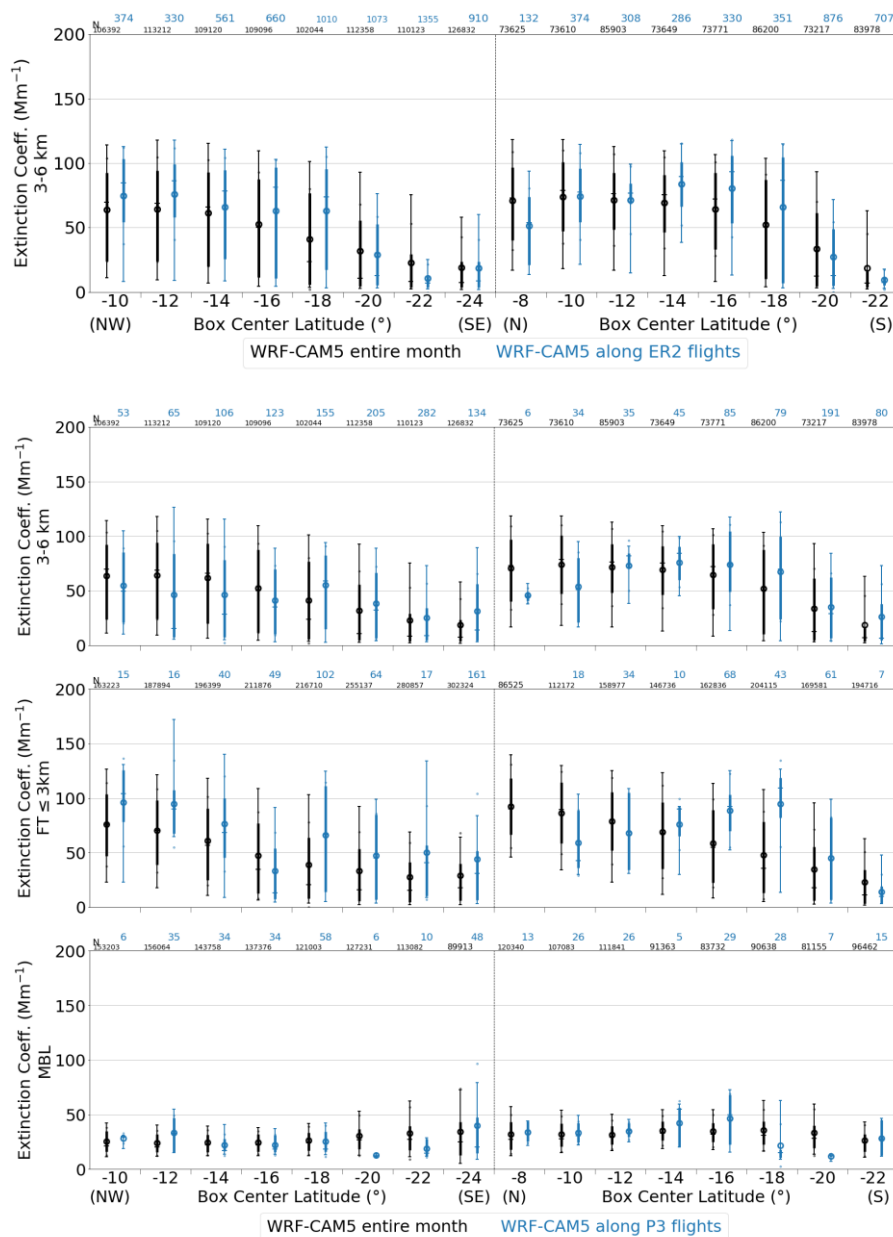
10

11

12

13

14



1

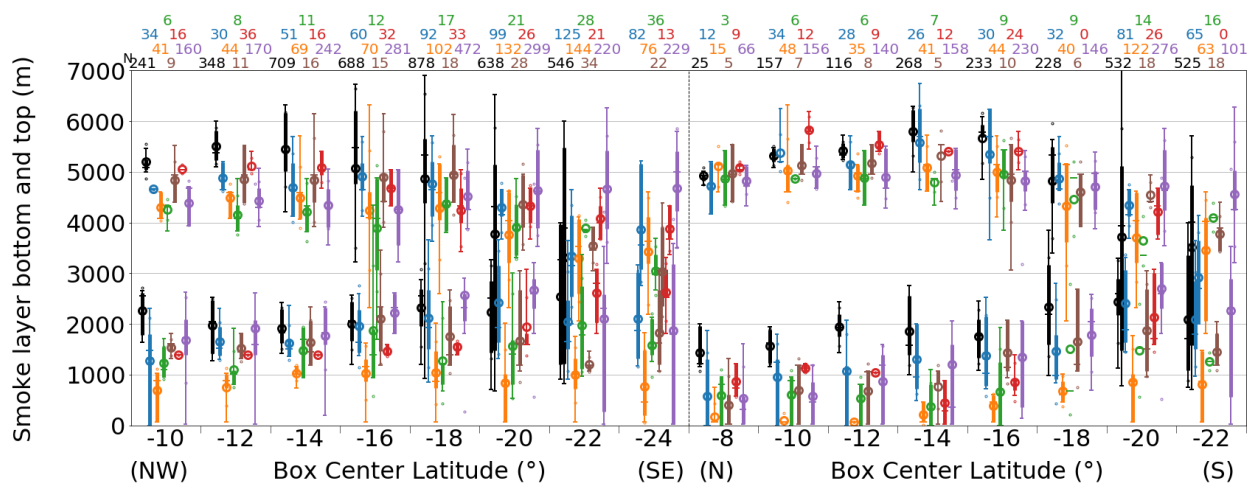
2 **Fig. 4.** Extinction coefficients compared between two extracts (monthly climatology and  
 3 flights) of WRF-CAM5 simulations. The top panel (a) is along the ER2 tracks for altitudes  
 4 between 3-6 km. The other three panels are for the P3 tracks for 3-6 km (b), the top of  
 5 MBL to 3 km (c) and the MBL (d). In each panel, the abscissa represents the eight



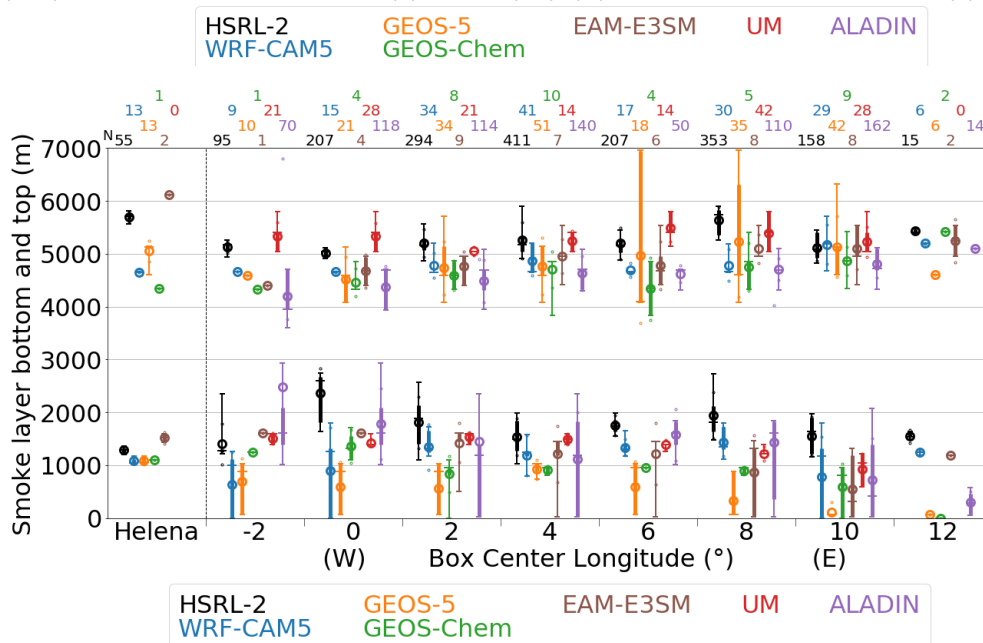
1 **diagonally aligned boxes and eight meridionally aligned boxes described in Section 3.2 and**  
2 **Fig. 2. In each box, the bars indicate the monthly climatology (black) and samples along the**  
3 **flights (blue). Distributions are represented as box-whisker plots encompassing the 10, 25,**  
4 **50, 75, and 90th percentiles, with circles indicating the mean and mean  $\pm$  standard**  
5 **deviation values. The numbers in small print on the top of each panel indicate the number**  
6 **of samples.**



1



2



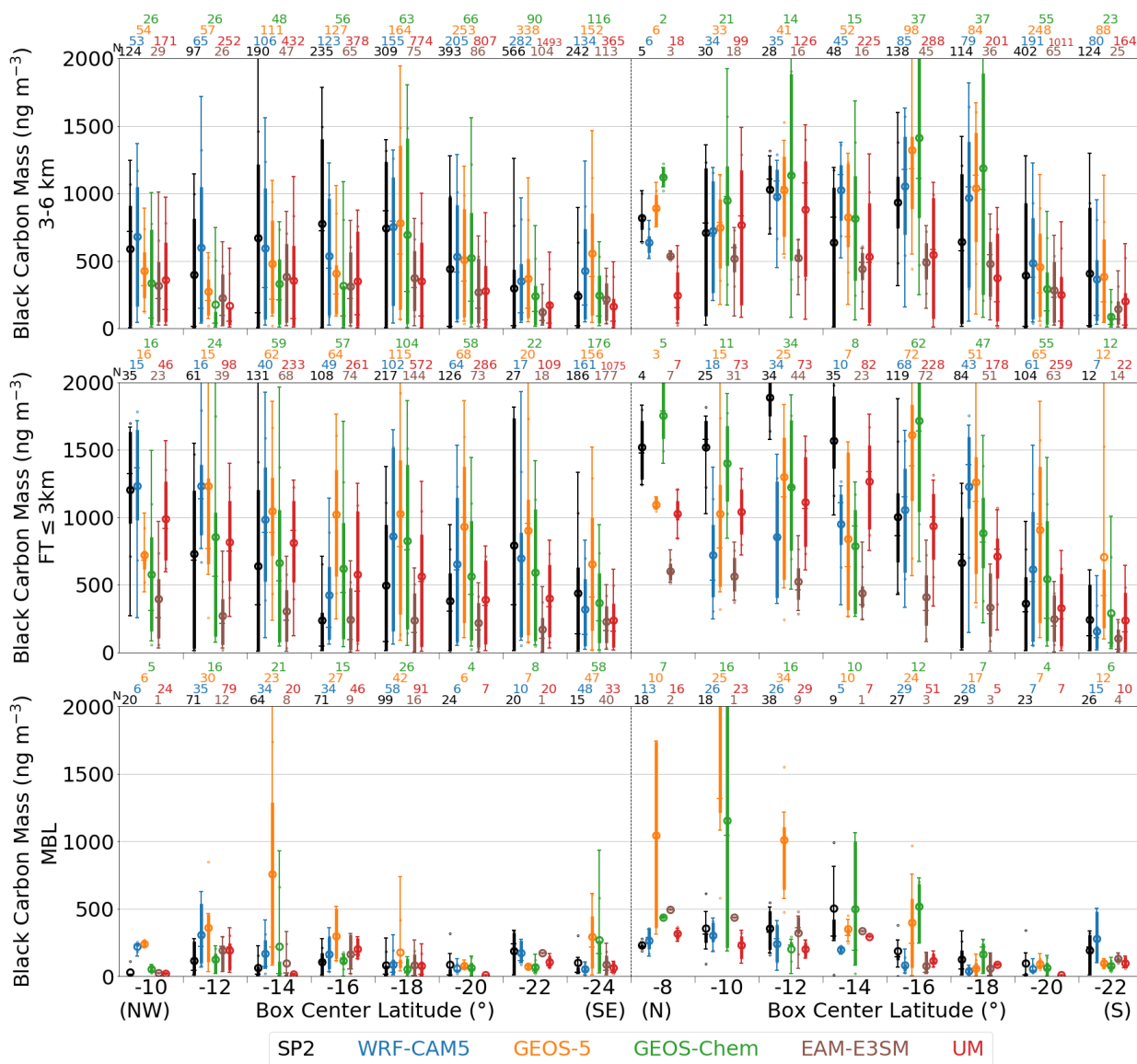
3

4 **Fig. 5. Smoke layer bottom and top altitudes. Smoke layers are identified through HSRL-2**  
 5 **backscatter intensities exceeding  $0.25 \text{ Mm}^{-1}\text{sr}^{-1}$ , ALADIN extinction coefficient exceeding  $17$**   
 6  **$\text{Mm}^{-1}$  and, for other models, BC mass concentration exceeding  $200 \text{ ng m}^{-3}$ . See Section 2.1**  
 7 **for details. The top panel (a) is for the diagonal and meridional corridors, while the bottom**  
 8 **panel (b) is for the St Helena Island and the zonal corridor. See Section 3.2 and Fig. 2. In**  
 9 **each box, the bars indicate the observations from the ER2 aircraft (black) and model**



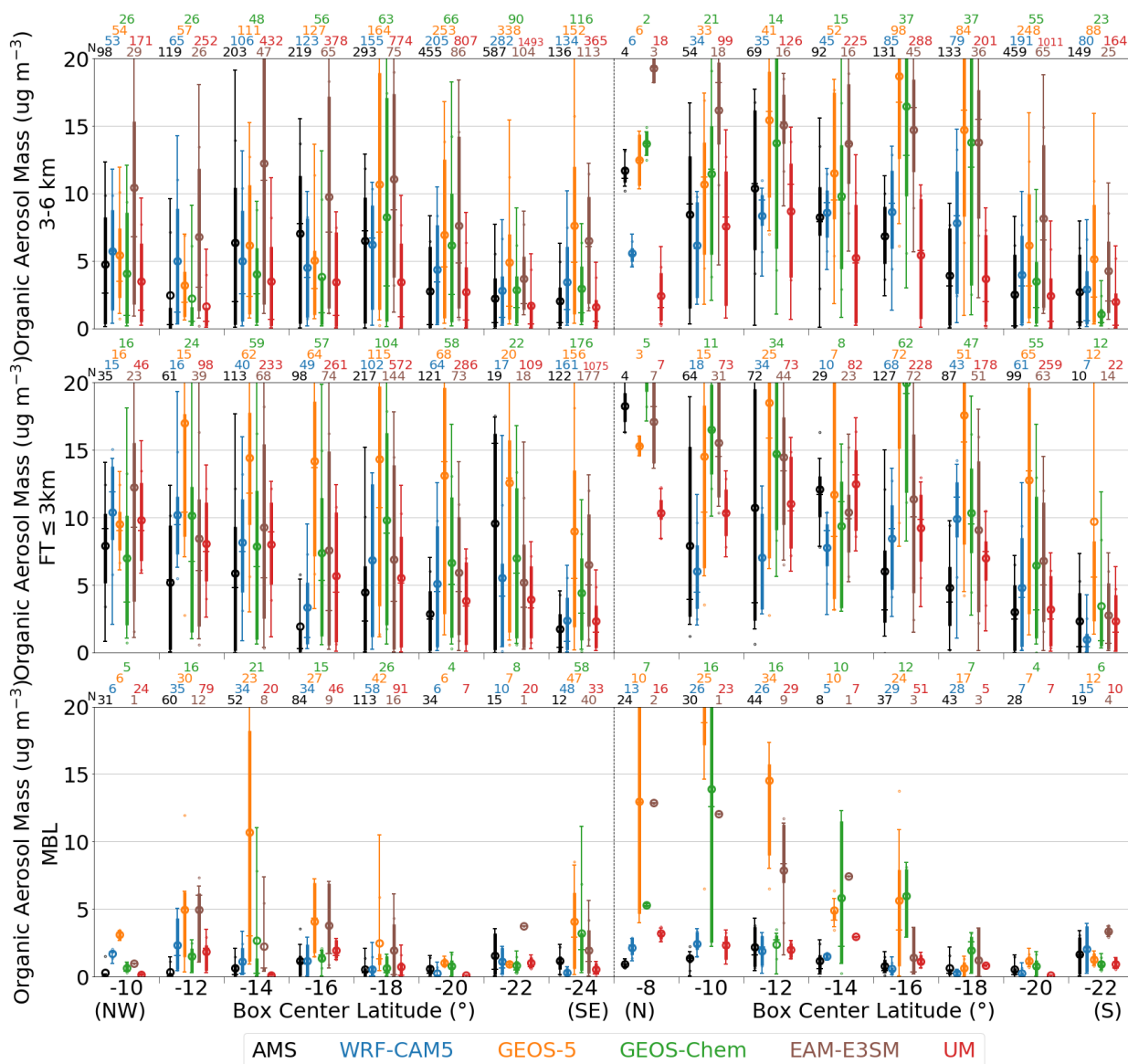
1 **products (colors). See Fig. 4 for a description of each bar and number. The model values**  
2 **presented here are sampled along the longitude, latitude and time of the flights. Missing box-**  
3 **whiskers indicate products unavailable.**

4



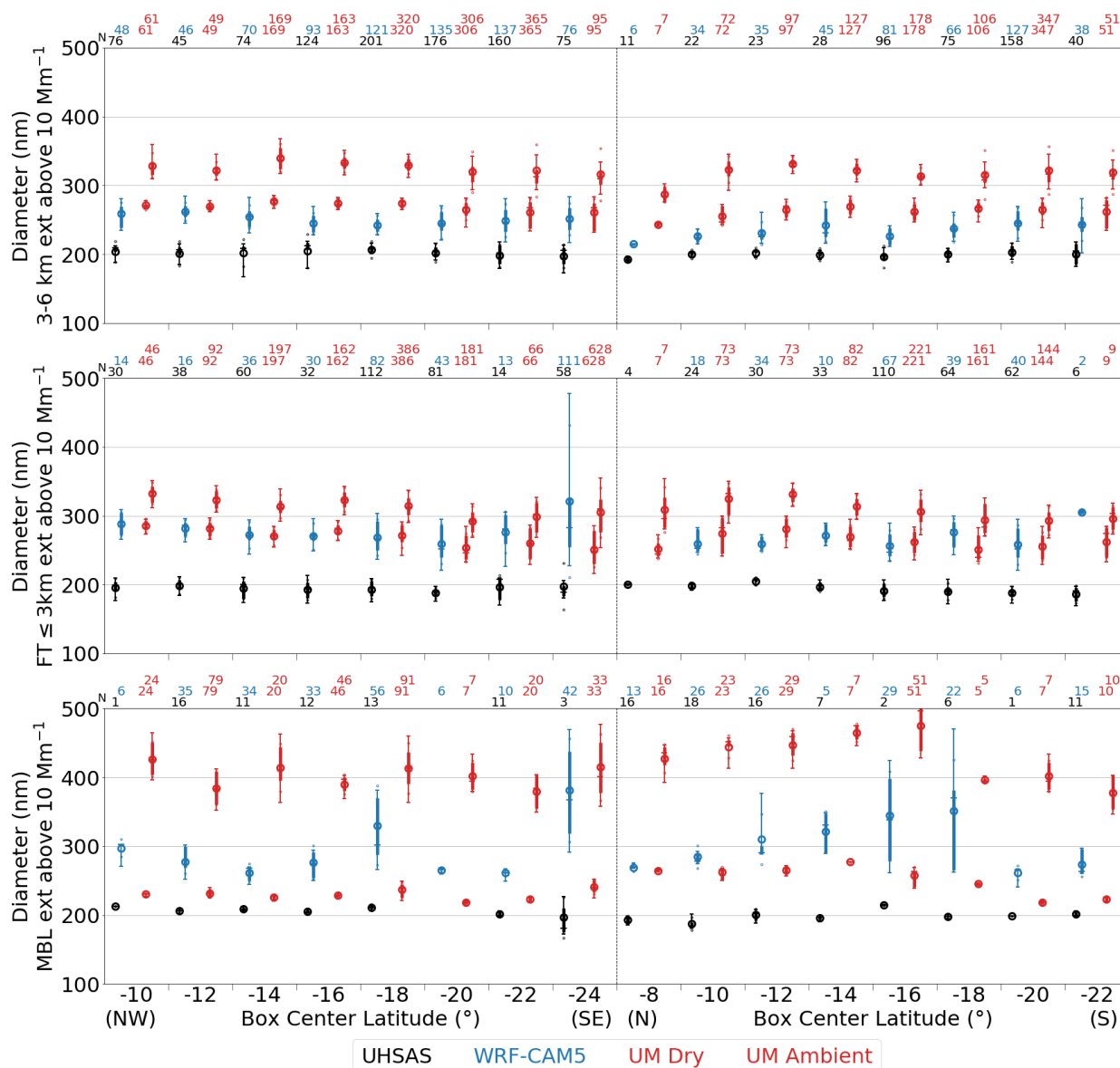
1

2 **Fig. 6. Black carbon mass concentrations compared between observations (black) and**  
 3 **models (colors), for (a) 3-6 km, (b) the top of MBL to 3 km and (c) the MBL. The left-hand**  
 4 **side of each panel corresponds to the eight diagonally-aligned boxes of the routine flight**  
 5 **path, and the right-hand side to the eight meridionally-aligned ones described in Section**  
 6 **3.2 and Fig. 2. See Fig. 4 for a description of each bar and number.**



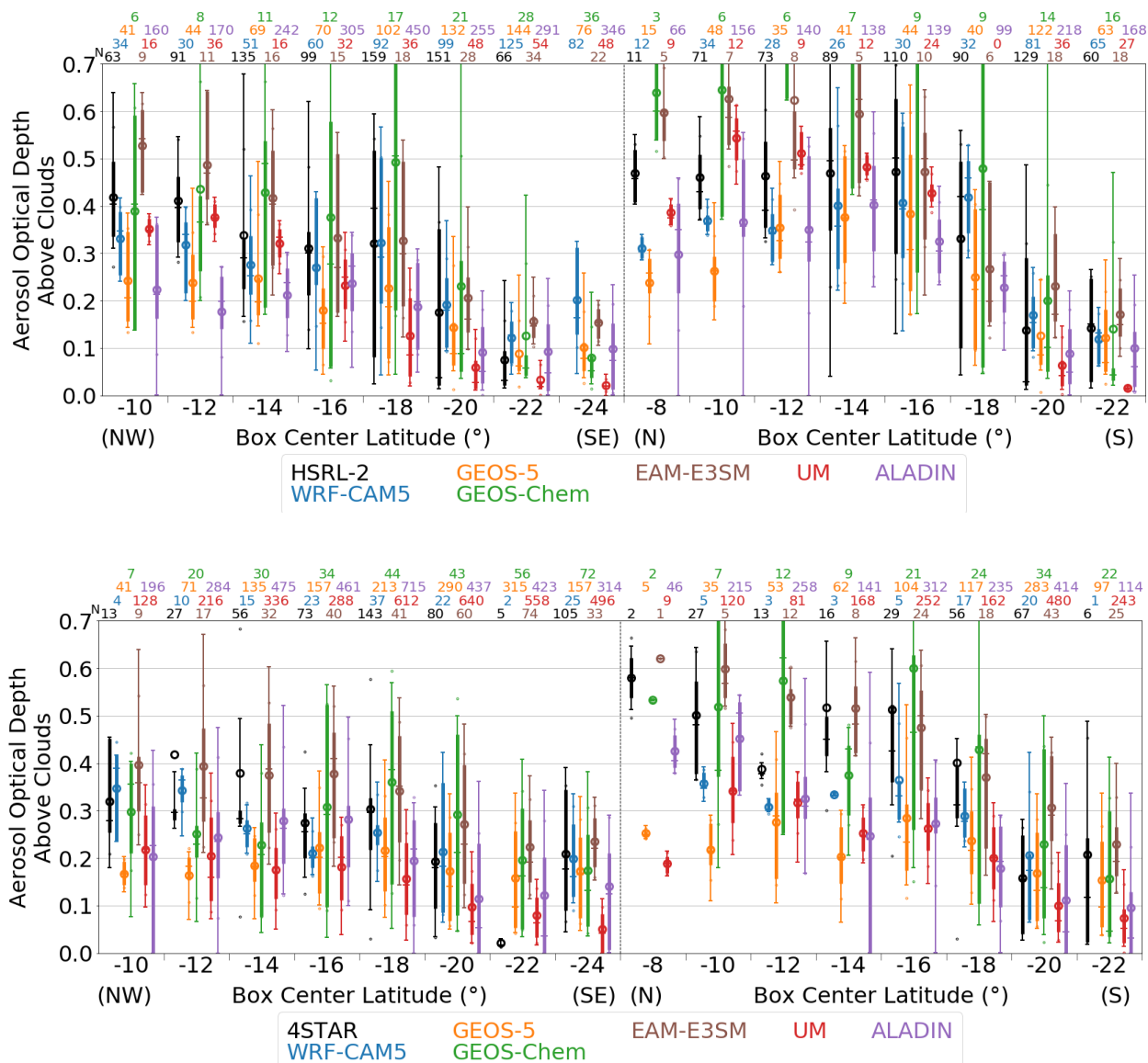
1  
 2 **Fig. 7. Same as Fig. 6 but for organic aerosol mass. The range of vertical axis is chosen for**  
 3 **clarity. The GEOS-5 mean values in two boxes exceed the range.**

4



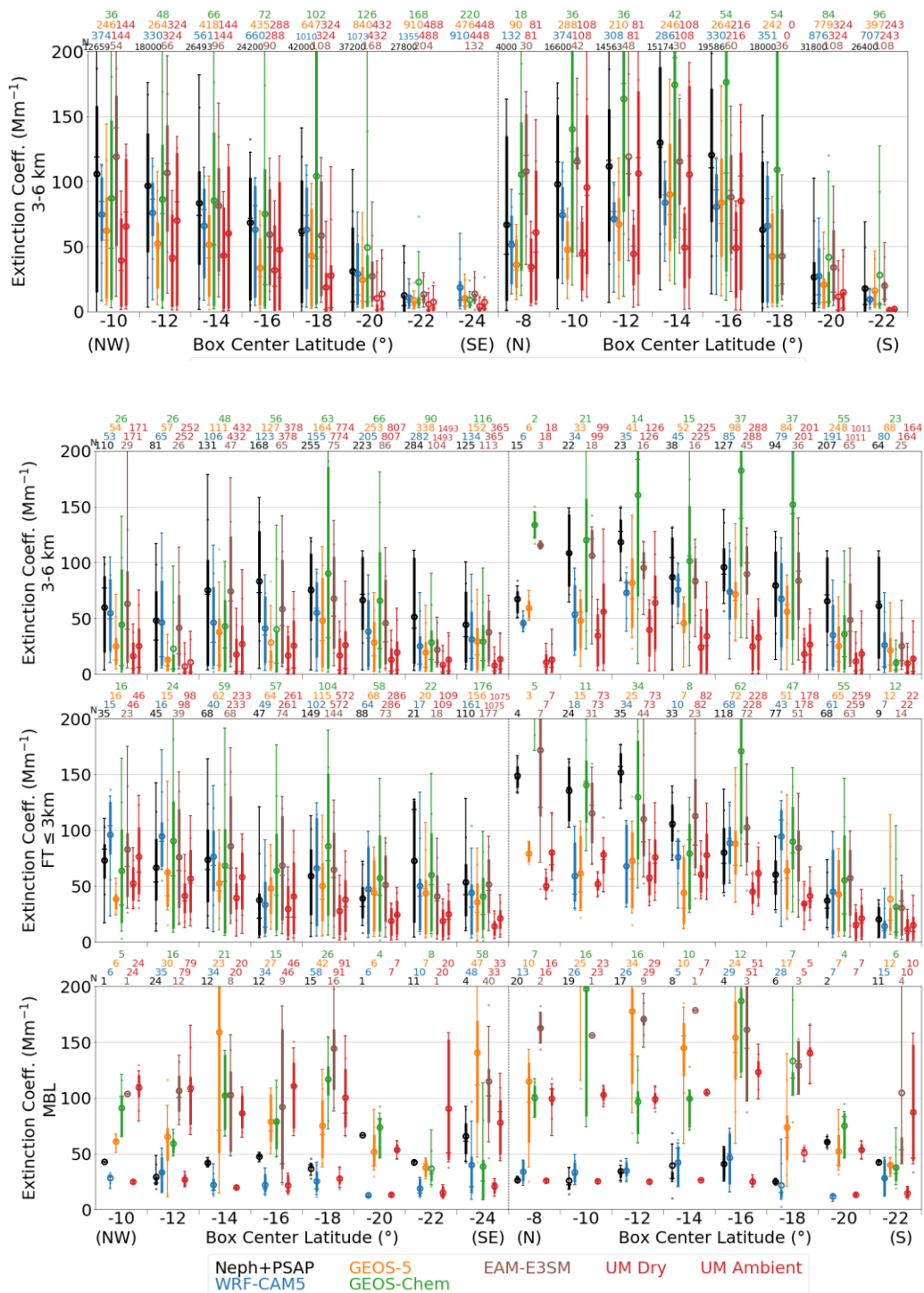
1

2 **Fig. 8.** Same as Fig. 6 but for dry volumetric mean diameter. Samples with 550 nm dry  
 3 extinctions less than  $10 \text{ Mm}^{-1}$  are excluded. For UM, the values for ambient RH conditions  
 4 are given to the right of the ambient ones.



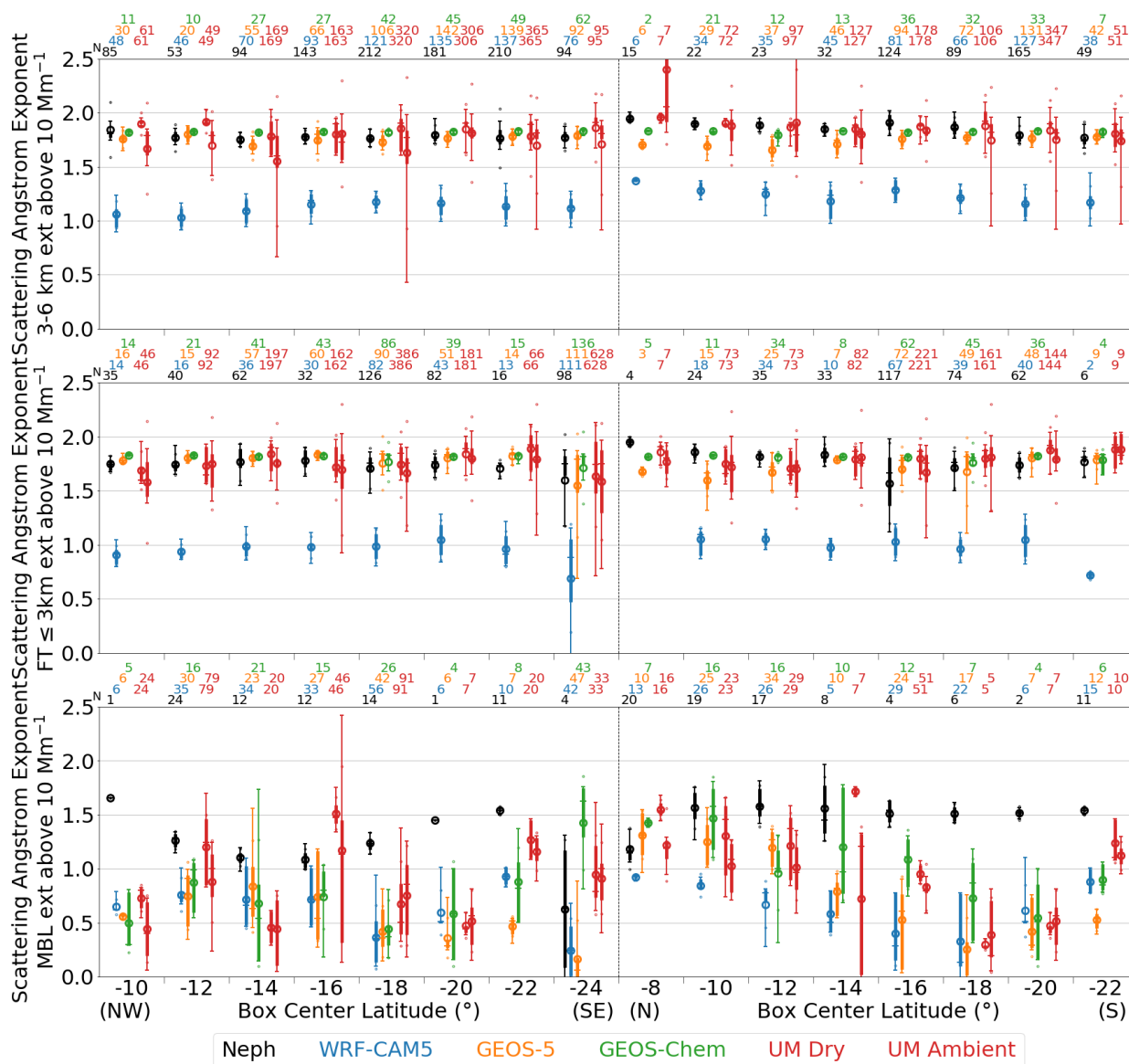
1

2 **Fig. 9.** The aerosol optical depth above clouds (AC-AOD) compared between  
 3 observations and models. The top panel (a) compares to the HSRL-2 lidar observation  
 4 from the ER2. The bottom panel (b) compares to the 4STAR measurements made while the  
 5 P3 aircraft was immediately above clouds.



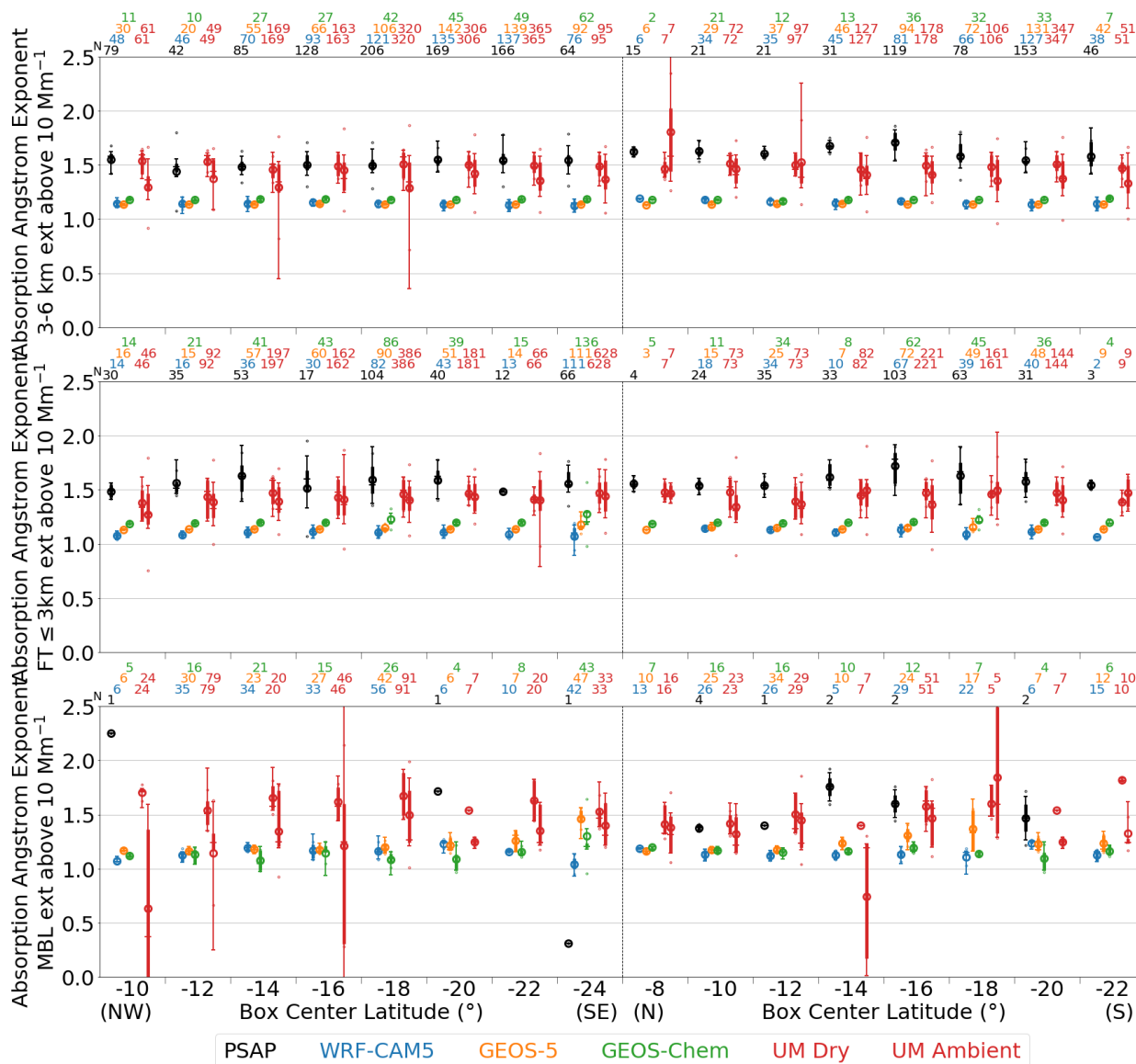


1 **Fig. 10. Extinction coefficients compared between observations and models. The top panel**  
2 **(a) compares to the HSRL-2 lidar observation of the ambient particles from the ER2 for 3-**  
3 **6 km. The other three panels compare to the nephelometer and PSAP measurements of**  
4 **dried particles aboard the P3 aircraft for (b) 3-6 km, (c) the top of MBL to 3 km and (d)**  
5 **MBL. For UM, the values for dry RH conditions are given to the left of the ambient ones.**



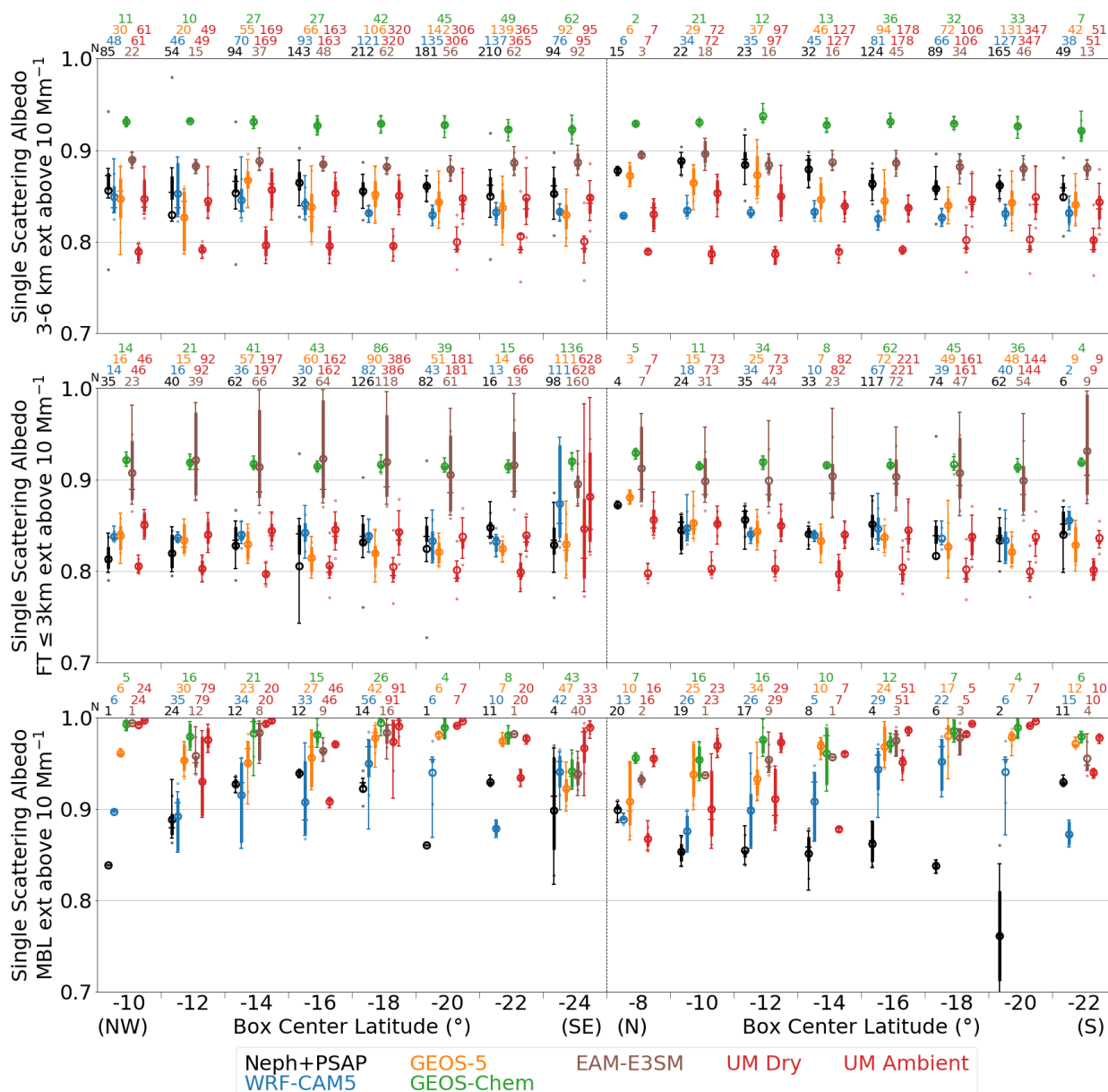
1  
 2 **Fig. 11. Same as Fig. 6 but for Scattering Ångström exponent.**

3



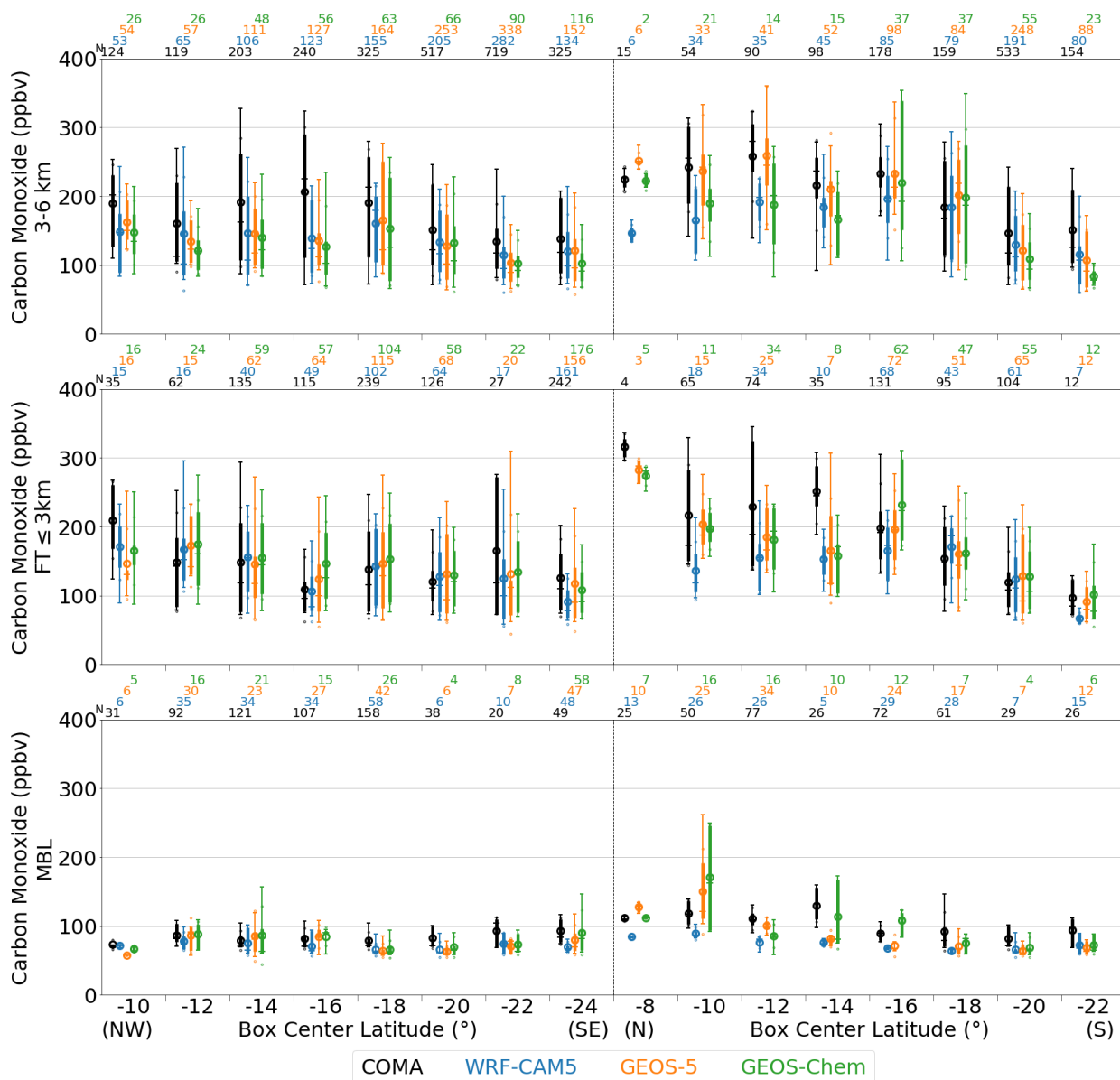
1  
 2 **Fig. 12.** Same as Fig. 6 but for Absorption Ångström exponent.

3



1  
 2 **Fig. 13.** Same as Fig. 6 but for SSA.

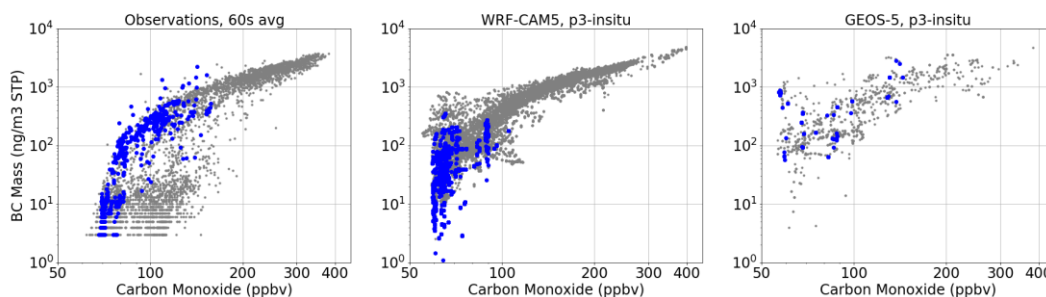
3



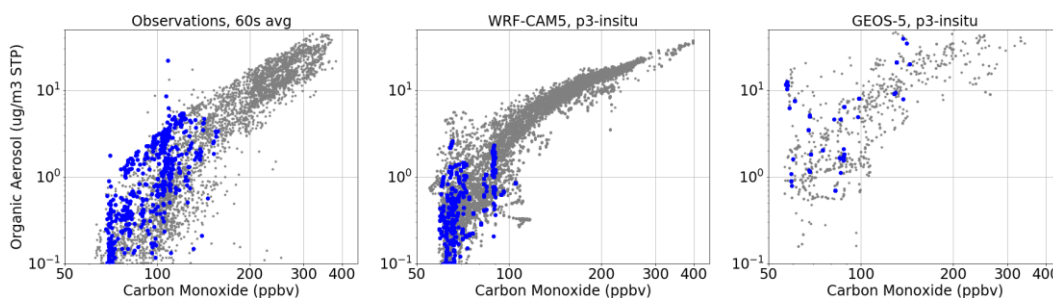
1  
 2 **Fig. 14.** Same as Fig. 6 but for carbon monoxide mixing ratio.



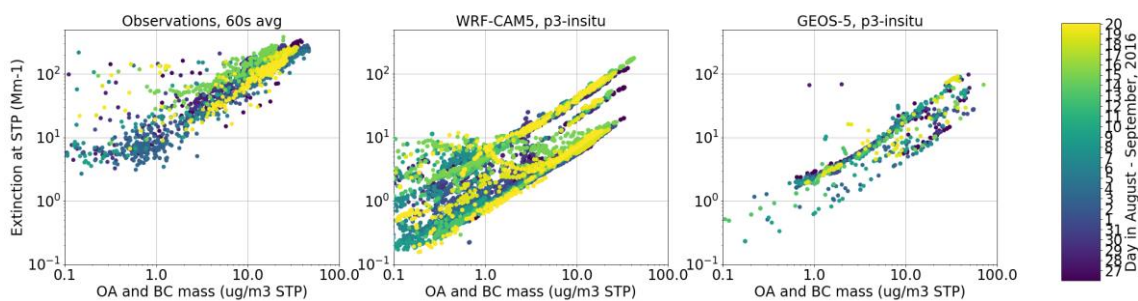
1



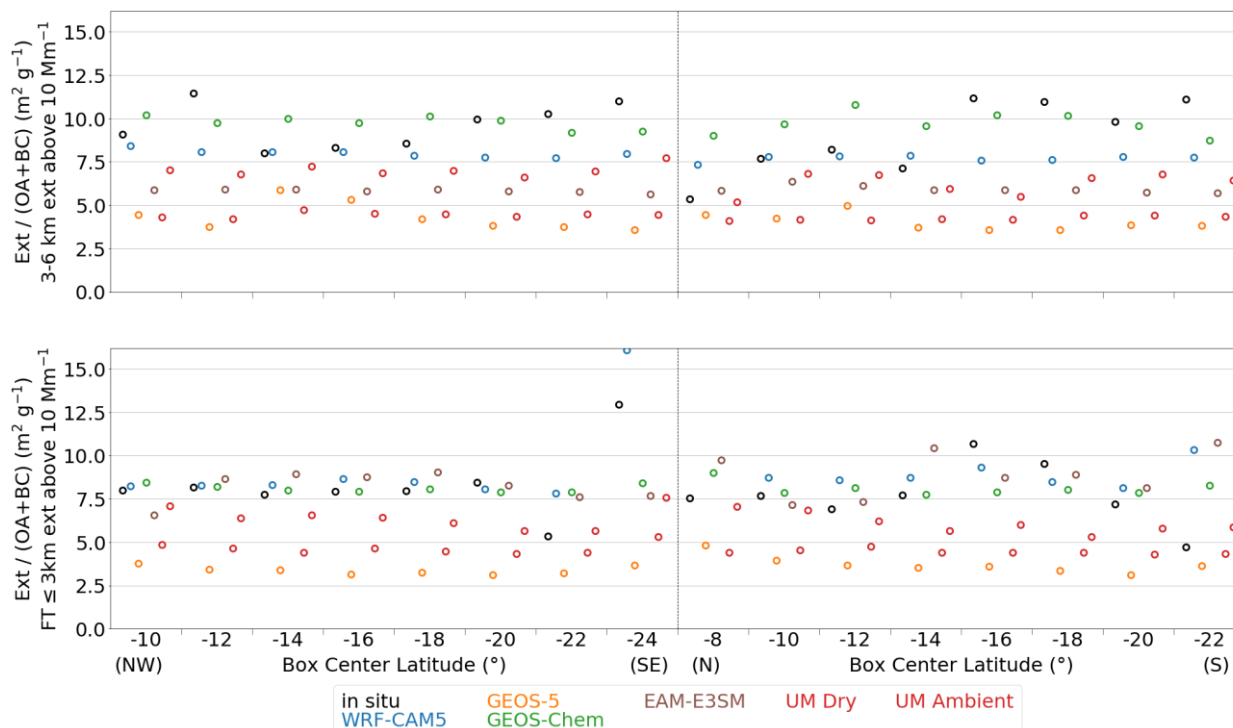
2



3



4 **Fig. 15. (a) Black carbon mass per air at 1013.25 hPa, 273.15 K compared with carbon**  
5 **monoxide mixing ratio on a 60s average basis for the observation in the FT (grey) and**  
6 **boundary layer (blue). (b, c) Same variables but from the WRF-CAM5 and GEOS-5**  
7 **models, respectively, sampled along the P3 flight tracks. (d, e, f) Same as the first row but**  
8 **with organic aerosol mass in place of BC mass. (g, h, i) The mid-visible light extinction by**  
9 **dried particles compared with the sum of OA and BC masses, for the FT only. The color**  
10 **indicates the day of measurements.**



1  
2 **Fig. 16.** The ratio of extinction to the sum of organic aerosol and black carbon masses,  
3 computed for box mean values. The in situ observation of extinction is for dried particles,  
4 while the models refer to ambient humidity conditions except for UM Dry. The top and  
5 bottom panels are for 3-6 km and for the top of boundary layer to 3 km, respectively.

6  
7